Journal of Asian Earth Sciences 220 (2021) 104914

Contents lists available at ScienceDirect

Journal of Asian Earth Sciences

journal homepage: www.elsevier.com/locate/jseaes

Genesis of carbonate-hosted Zn-Pb deposits in the Late Indosinian thrust and fold systems: An example of the newly discovered giant Zhugongtang deposit, South China

Chen Wei [a,b], Zhilong Huang [a,*], Lin Ye [a,*], Yusi Hu [a], M. Santosh [c,d], Tao Wu [a,b], Lianglun He [e], Jiawei Zhang [a,f], Zhiwei He [g,h], Zhenzhong Xiang [a,b], Da Chen [i], Chuanwei Zhu [a], Zhongguo Jin [i]

[a] State Key Laboratory of Ore Deposit Geochemistry, Institute of Geochemistry, Chinese Academy of Sciences, Guiyang 550081, China
[b] University of Chinese Academy of Sciences, Beijing 100049, China
[c] School of Earth Sciences and Resources, China University of Geosciences, Beijing 100083, China
[d] Department of Earth Science, University of Adelaide, Adelaide, SA 5005, Australia
[e] 113 Geological Team, Bureau of Geology and Mineral Exploration and Development of Guizhou, Liupanshui 553000, China
[f] Guizhou Geological Survey, Bureau of Geology and Mineral Exploration and Development, Guiyang 550081, China
[g] College of Earth Sciences, Chengdu University of Technology, Chengdu 610059, China
[h] Guiyang Mining Development and Investment Co. Ltd, Guiyang 550000, China
[i] Institute of Geology and Mineral Resource Exploration, Non-Ferrous Metal and Nuclear Industry Geological Exploration Bureau, Guiyang 550005, China

ARTICLE INFO

Keywords:
In-situ trace elements in pyrite
In-situ S-Pb isotopes
Bulk C-O isotopes
Sources of metal elements and associated fluid
MVT deposit in thrust belt

ABSTRACT

The Sichuan-Yunan-Guizhou triangle region contains numerous economically important carbonate-hosted Zn-Pb deposits that occur in the Late Indosinian thrust and fold system rather than foreland basin. In this paper, we investigate the thrust-controlled Zhugongtang deposit (>30.0 Mt ores @ 6.76 wt% Zn and 2.27 wt% Pb) as a case study, using ore deposit geology, in-situ trace elements and isotopes in sulfides, to provide new insights into the ore genesis of the MVT deposits in the thrust belts. The sulfide orebody is structurally controlled by a kilometer-scale thrust system and occurs as open-space fillings, vein or replacement structures. Trace elements in pyrite show a low concentration of Co, Ni, Tl and Se, suggesting that the sulfides were formed under low-temperature (100–250 °C) and slightly reduced conditions. The $\delta^{13}C_{PDB}$ values (−7.53 to +1.73‰) in calcite lie between the marine carbonate rocks and sedimentary organic matter, and the calculated $\delta^{18}O_{fluid}$ values (+3.40 to +13.36‰) are different from that of marine carbonate rocks but partly overlap with the basinal brines. Such C-O isotope signature indicates that the carbon was mainly derived from the host rocks (limestone) with additional contribution from organic carbon. The oxygen isotope values suggest mixing of the basinal brine and the limestone. The $\delta^{34}S$ values of sulfides within Permian strata (+12.2 to +15.3‰) and Devonian strata (+18.5 to +23.8‰) are similar to the coeval seawater sulfate within the ore-hosting strata, respectively. This indicates that the reduced sulfur is originated from evaporative sulfate within host rocks by thermo-chemical reduction in the near-close system. In-situ Pb isotopic ratios of galena ($^{206}Pb/^{204}Pb$ = 18.566–18.758, $^{207}Pb/^{204}Pb$ = 15.757–15.769 and $^{208}Pb/^{204}Pb$ = 39.061–39.366) are comparable with the Proterozoic basement and the country rocks, indicating the mineralizing metals were mainly derived from basement rocks and partly extracted from country rocks via fluid-rock interaction. Regional geological evidence indicates the timing of Zn-Pb mineralization of Zhugongtang is Late Triassic to Early Jurassic and related to the Indosinian orogeny. Overall, the newly obtained trace element and isotopic data together with geological evidence suggest that the Zhugongtang deposit is an MVT deposit formed in the orogenic thrust belt and that fluid mixing was critical for the ore formation.

1. Introduction

Mississippi valley-type (MVT) deposits which constitute one of the important sediment-hosted Zn-Pb deposits with no genetic link with igneous activity, host 16–17% of the known global lead and zinc resources (Singer, 1995; Leach et al., 2005). These deposits are hosted by

* Corresponding authors.
E-mail addresses: huangzhilong@vip.gyig.ac.cn (Z. Huang), yelin@vip.gyig.ac.cn (L. Ye).

https://doi.org/10.1016/j.jseaes.2021.104914
Received 30 May 2021; Received in revised form 26 July 2021; Accepted 1 August 2021
Available online 3 August 2021

carbonate rocks, with a mineral assemblage dominated by sphalerite, galena, and/or fluorite and the hydrothermal fluid associated with the mineralization is low-temperature (90–150 °C) with high salinities (10–30 wt% NaCl eqv.) basinal fluid (Anderson and Macqueen, 1982; Leach et al., 2005). Diverse region-specific names (or subtypes) have been coined for the deposit types (such as Appalachian-, Bleiberg-, Silesia- and Irish-type) based on the diversity of deposit morphology and ore-forming environments (Leach et al., 2005). The formation of these deposits is mainly controlled by the tectonic setting such as (i) classic orogenic foreland basins (Appold and Garven, 1999; Leach et al., 2001), and (ii) rifts in extensional environments (Bau et al., 2003; Partey et al., 2009) and (iii) thrust and fold belts (Smethurst et al., 1999; Song et al., 2015; Liu et al., 2017). The available genetic models indicate that the deposits formed in orogenic foreland basins with low-temperature of 90–150 °C that are associated with large-scale basinal fluid migration driven by the regional compressional tectonic events (Leach et al., 2001, 2005; Bradley and Leach, 2003). The relatively high-temperature (130–270 °C) deposits formed in extensional environments and may be related to metal-rich basinal fluid that circulated deep into basement lithologies (e.g., Heijlen et al., 2003; Muchez et al., 2005; Wilkinson, 2010). In contrast, the ore genesis of MVT deposits formed in orogenic thrust belts are poorly investigated and understood, and the sources of sulfur and metals and the ore-forming process and/or metal precipitation mechanisms involved remain unclear and controversial (Bradley and Leach, 2003).

The Sichuan-Yunnan-Guizhou triangle region is an ideal area for studying thrust-hosted epigenetic Zn-Pb deposits by virtue of the multistage terrane collision history from Early Neoproterozoic to Cenozoic and is a major region for economically important carbonate-hosted Zn-Pb deposits (>200 Mt sulfide ores, grading 10–35% Pb + Zn for all deposits; e.g., Zhang et al., 2015; Zhou et al., 2018) within orogenic thrust belt. Although several studies were conducted on the carbonate-hosted Zn-Pb deposits in the Sichuan-Yunnan-Guizhou Metallogenic Province (SYGMP) to document their geological characteristics, mineralization age, ore genesis and tectonic setting (Liu and Lin, 1999; Huang et al., 2004; Han et al., 2012; Zhang et al., 2015; Zhou et al., 2018; Oyebamiji et al., 2020 and reference therein), many issues, particularly the ore genesis and the tectonic setting, remain unclear. These deposits have high ore grade (>10 wt% Pb + Zn), high mineralizing temperature (120–260 °C) and show spatial and genetic association with igneous activities of the Emeishan large igneous province (ELIP), leading to some authors correlating these with the SYG-type (e.g., Zhou et al., 2013a,b, 2018 and reference therein). Others proposed Huize-type based on the geometry of orebodies (fault-controlled pipe-like), ore grade (>10 wt% Pb + Zn) and based on the feature that the compressional tectonic setting of these deposits are different from that of MVT deposits formed in the foreland basins (e.g., Han et al., 2012, 2014). In addition, several studies consider these deposits as MVT deposits based on the timing of mineralization and the geological evolution of the SYG area (e.g., Wu et al., 2013; Zhang et al., 2015).

In this study, we investigate the newly discovered thrust-hosted Zhugongtang deposit in the SYGMP and apply multiple techniques of scanning electron microscope (SEM), laser ablation inductively coupled plasma mass spectrometry (LA-ICPMS) in-situ trace element in pyrite, bulk C-O and LA-Multicollector(MC)-ICPMS in-situ S-Pb isotopes for the deposit. The main objectives of this study are to (i) evaluate the nature of hydrothermal fluids and the source(s) of ore-forming elements, (ii) decipher the ore-forming process and sulfide precipitation mechanisms, and (iii) constrain the timing of Zn-Pb mineralization and its relation to the regional tectonic events. The new data together with the detailed dataset of the ore deposit geology and mineralogy provide insights into the ore genesis of the Zhugongtang deposit, and a better understanding of the formation of thrust-hosted Zn-Pb deposits in the Yangtze Block, and elsewhere.

2. Geological setting

The Yangtze Block in South China experienced multiple tectonic events and has been described in detail by Metcalfe (2006) and Wang et al. (2013). The Yangtze and Cathaysia blocks were amalgamated along the Jiangnan suture at around 850–820 Ma (e.g., Dong et al. 2012; Yao et al. 2014). Subsequently, the Early Paleozoic Wuyi–Yunkai orogeny occurred in South China Block, resulting in the remobilization of the basement of the eastern Yangtze and Cathaysia blocks (Li et al., 2010; Yao and Li, 2016). In the early Triassic, South China Block collided with North China and Indochina blocks to the north and south (e.g., Matcalfe, 2002; Cawood, 2005). During the early to middle Jurassic, the South China Block was dominated by extension in response to the westward subduction of the Pacific plate beneath SE China (Wang et al., 2013).

In the SW Yangtze Block, the SYGMP encompasses a total area of about 170,000 km^2 and is confined by three regional fault belts, namely the NW-trending Kangdian–Yiliang–Shuicheng, the NS-trending Anninghe–Lvzhijiang and the NE-trending Mile–Shizong–Shuicheng fault belt (Fig. 1). These faults extend into the basement rocks and were continually activated or reactivated by the multiphase orogenic activities (e.g., Wuyi-Yunkai, Indosinian and Yanshanian) within South China Block (e.g., Huang et al., 2004). Regional stratigraphy comprises a Mesoproterozoic folded meta-sandstone and slate basement and overlain by Paleozoic to Early Mesozoic submarine sedimentary sequences and Jurassic to Cenozoic terrigenous sedimentary sequences. Mesoproterozoic basement consists of the Dongchuan (1.7–1.5 Ga) and Kunyang (0.95–1.0 Ga) Groups and equivalents that mainly comprise greywackes, slates, and other carbonaceous to siliceous sedimentary rocks with ~20 km thickness (Li et al., 1984). The following strata are composed of Neoproterozoic to the Lower Permian submarine carbonate rocks and clastic sedimentary sequences in a passive continental margin (e.g., Yan et al., 2003). The Lower Ediacaran units are mainly volcanic clastic rocks and dolostone rock (the uppermost part). The Cambrian strata dominantly consist of black shales and sandstones interlayered with dolostone and limestone. Ordovician sediments are dominantly composed of limestone, dolostone and shale, conformably overlain by Silurian strata dominated by fine-grained sandstones, shales, and carbonate rocks. Following this are Devonian sediments, which dominantly comprise sandstone, calcareous sandstone, shale, limestone and dolostone. Carboniferous strata consist of limestone, oolitic limestone and dolostone. The Lower Permian sediments comprise limestone, dolostone and argillaceous siltstone, which is unconformably overlain by the Permian Emeishan flood basalts, which are a product of the ELIP (~260 Ma; He et al., 2007).

The SYGMP hosts numerous Zn-Pb deposits that commonly occur in Neoproterozoic to Early Permian carbonate strata. In particular, the Late Ediacaran Dengying and Early Carboniferous formations (Fms) account for >62% of proven Zn-Pb deposits and ~70% of metal reserves (Liu and Lin 1999; Huang et al., 2004). These sulfide ores occur as stratiform, lenticular and pipe-like orebodies controlled by thrust and fold systems. The salient characteristic of the primary ore deposits in the SYGMP have summarized in Table 1.

3. Geology of the Zhugongtang deposit

3.1. Stratigraphy and lithology

The newly discovered Zhugongtang deposit, located in the NW part of the Hezhang county, is the largest Zn-Pb deposit in Guizhou (He et al., 2019). The dominant rocks exposed in the region are mainly Early Silurian to Late Permian sedimentary cover (Figs. 2 and 3; He et al., 2019). The oldest rock in the Zhugontang mining area is Early Silurian Hanjiadian Fm (S_1h) sandstone and silty mudstone, unconformably overlain by Devonian Wangchengpo and Yaosuo Fms (D_3w-y) that is composed of dolostone, siliceous dolostone, limestone and dolomitic

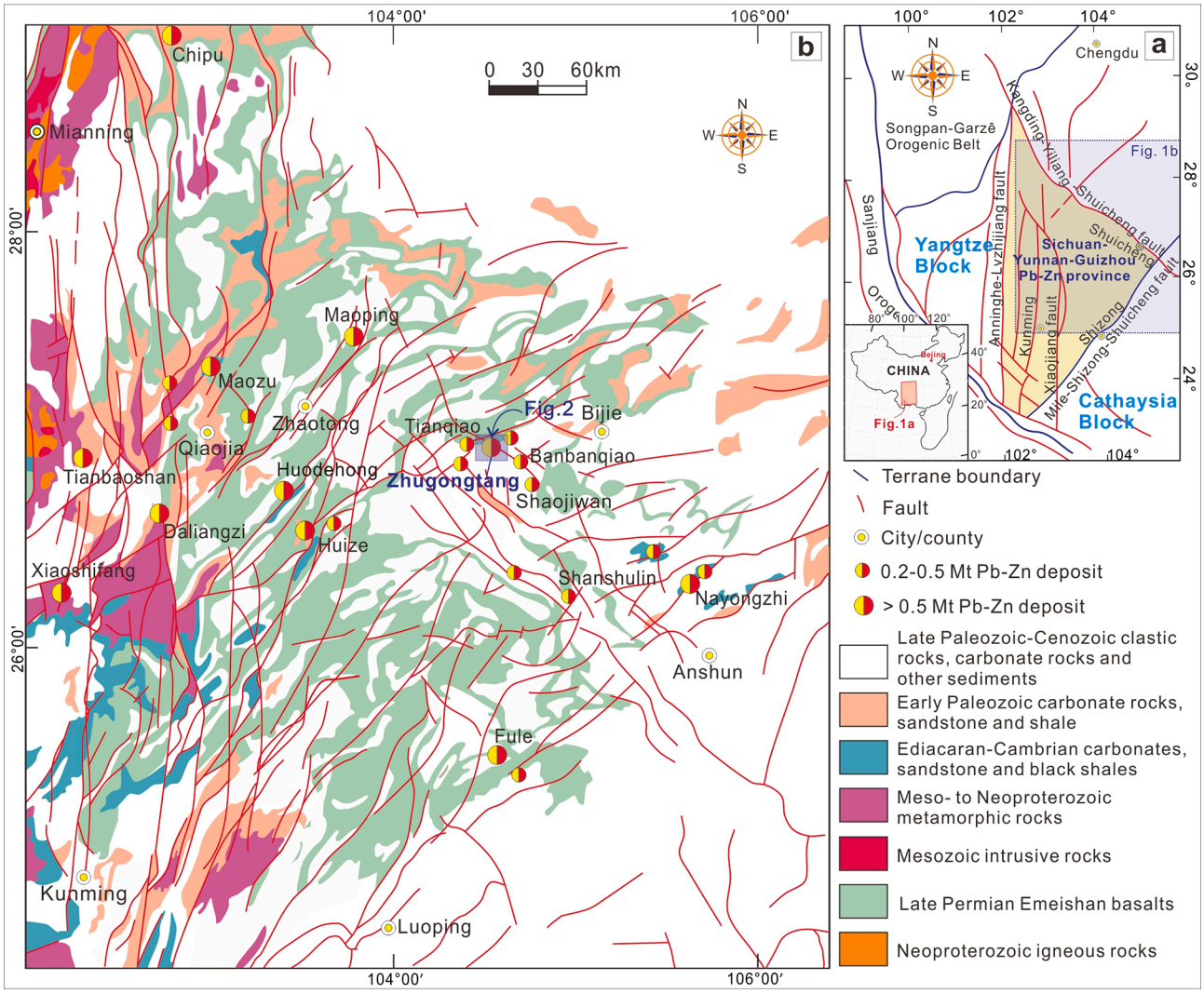

Fig. 1. (a) Simplified tectonic map showing the location of the Sichuan-Yunnan-Guizhou Metallogenic province (SYGMP) in the western Yangtze Block, South China, (b) Geological map of the SYGMP showing regional structures, strata and the distribution of Zn-Pb deposits (modified from Liu and Lin, 1999; Zhou et al., 2018).

limestone (secondary ore host). The Devonian Yaosuo Fm (D_3y) is overlain unconformably by the Carboniferous and Permian strata that include: (i) Lower Carboniferous Xiangbai Fm (C_1x) limestone, calcareous shale and dolostone, (ii) Lower Carboniferous Jiusi, Shangsi and Baizou Fms (C_1j-b) limestone, dolomitic limestone, shale and dolostone, (iii) Upper Carboniferous Huanglong and Maping Fms (C_2h-m) limestone, dolomitic limestone, bioclastic limestone and dolostone, (vi) Lower Permian Liangshan Fm (P_1l) sandstone, calcareous shale and argillaceous siltstone, (v) Lower Permian Qixia and Maokou Fms (P_1q-m) limestone dolomitic/bioclastic limestone (main ore host), (vi) Late Permian Emeishan Fm ($P_2\beta$) (unconformably overlies the Maokou Fm) flood basalts and (vii) Late Permian Longtan Fm (P_3l) sandstone, shale and claystone.

3.2. Structure

The major structural features at Zhugongtang are NW-, NE- and EW-trending faults (Fig. 2) and minor interlayer fracture (Fig. 2). The steep NW-trending thrust faults (F1, F2 and F3) show a subparallel trend in the transverse profile, forming the Yadu-Mangdong imbricate structure (Fig. 2). The F1 thrust fault strikes NE 315°and has steep (45–70°) SW dip with the fault/fracture zone with a width of 0.5–25 m. The F2 thrust fault (parallel to fault F1) is ~9.8 km long and trends SW with a steep dip of 45–70° with 1–60 m wide fault/fracture zone, which is the main ore host. The F3 thrust fault (displaying similar strike with F1 and F2 faults) is 6.5 km and has a steep angle (45–70°) and SW dip, which is separated into three parts by NE-trending post-ore faults and final merges with F2 fault. The post-ore F4 fault strikes NW and displays a normal fault charter, which cuts the orebody IV in the PD1 tunnel (He et al., 2019).

3.3. Zn-Pb mineralization

Orebodies in the Zhugongtang deposit mainly occur as stratiform, lenticular and steeply dipping veins within the NW-trending F1 and F2 faults and the interlayer fracture zones of F20 and F30 hidden faults (Fig. 4). Drilling, trenching and test shafts have discovered 69 different size orebodies which are grouped into six ore clusters (Nos. I–VI). The total base metal reserve of these ore clusters is ~3.27 Mt with a grade averaging 6.76 wt% Zn and 2.27 wt% Pb, associated with 828 t Ag at 43.4 g/t, 4992 t Cd at 174 g/t, 2.61 t Ga at 21.0 g/t, 612 t Ge at 36.0 g/t (He et al., 2019). Ore cluster Nos. I, III, V and VI occur in the interlayer fracture zones of the Lower Permian Qixia Fm (Fig. 4a and b) accounting for 75.27% of total metal resources. Ore cluster Nos. II and IV are hosted within the interlayer fracture zones of the Early Devonian Yaosu–Wangchengpo Fms (Fig. 4c) and account for 24.73%. Among these orebodies, orebody I-1, the largest orebody at Zhugongtang, is hosted in the fracture zones of the F1 fault and accounts for 65.90% of total metal resources. The orebody is 2300 m long, 300 m wide and 0.63–64.45 m

Table 1
Basic geological characteristics of the primary ore deposit in the Sichuan-Yunnan-Guizhou Metallogenic province (SYGMP).

Deposit	Host rocks	Reserves and grade (Zn + Pb)	Metal association	Morphology of orebodies	Ore-controlling structure	Ore texture	Mineral assemblage	Ore-forming fluids	mineralizing age (Ma)	References
Northwestern Guizhou										
Zhugongtang	Permian	>3.27 Mt, 1.0–35 wt%	Zn-Pb-Ga-Ge-Cd	Stratiform, lenticular, and steeply pipe	NW-trending thrust faults	Disseminated, massive, vein	Ore minerals: sphalerite, galena, pyrite; gangue minerals: dolomite, calcite and minor quartz and K-feldspar	Th:120–240 °C; sal: 2.1–12.9 wt% NaCl eqv.	No data	He et al., 2019; This study
Nayongzhi	Lower Cambrian dolostone	1.52 Mt, 4.6–7.5 wt%	Zn-Pb-Ga-Ge-Cd	Stratabound and bed-like	NE-trending anticline and faults	Disseminated, massive, brecciated	Ore minerals: sphalerite, galena and minor pyrite; gangue minerals: dolomite and calcite	Th:100.5–165.4 °C; sal: 1.2–18.6 wt% NaCl eqv.	458.5	Jin et al., 2016; Wei, 2018
Shaojiwan	Permian and Devonian dolostone	>0.3 Mt, 10–15 wt%	Zn-Pb-Ag	Lentiform and steeply dipping vein	NW-trending thrust faults	Massive, banded, disseminated and vein	Ore minerals: sphalerite, galena and pyrite; gangue minerals: dolomite, calcite with minor quartz	Th:115–170 °C; sal: 0.9–17.5 wt% NaCl eqv.	No data	Zhou et al., 2013a, 2018
Tianqiao	Devonian and Carboniferous dolostone	0.4Mt,15–18 wt %	Zn-Pb-Ag-Ge-Cd-Ag	Stratabound and lenses	NNW-trending thrust-fold	Massive, disseminated, banded	Ore minerals: sphalerite, galena and pyrite; gangue minerals: dolomite, calcite	Th:150–270 °C; sal: 9.6–14.2 wt% NaCl eqv.	191.9	Zhou et al., 2013b, 2018
Northeastern Yunnan										
Huize	Carboniferous dolostone	>7.0 Mt, >25 wt%	Zn-Pb-Ag-Ge-Ga-Cd	Stratabound, veins and lenses	NE-trending thrust faults	Massive, disseminated	Ore minerals: sphalerite, galena and pyrite; gangue minerals: dolomite, calcite and minor quartz	Th:165–220 °C; sal:6.0–12.0 wt% NaCl eqv.	220;	Huang et al., 2004; Li et al., 2006; Han et al., 2012
Maoping	Devonian and Carboniferous dolostone	>3.0 Mt, 15–30 wt%	Zn-Pb-Ag-Ge-Ga-Cd	Vertical pipe-like	NNE to NE-trending thrust-fold	Massive, disseminated	Ore minerals: sphalerite, galena and pyrite; gangue minerals: dolomite, calcite and minor quartz	Th:123–220 °C; sa:6.0–12.0 wt% NaCl eqv.	202.5	Han et al., 2012; Wei et al., 2021
Maozu	Late Ediacaran Dengying Fm. dolostone	~2.0 Mt, 12–14 wt%	Zn-Pb-Ga-Cd-Ag	Stratabound and lenses	NNE to NE-trending thrust-fold	Massive, disseminated, brecciated	Ore minerals: sphalerite, galena and pyrite; gangue minerals: dolomite, calcite and minor quartz	Th:153–248 °C; sal:2.8–5.3 wt% NaCl eqv.	196	Zhang et al., 2015; Li et al., 2020
Lehong	Late Ediacaran Dengying Fm. dolostone	2.4 Mt, >15 wt %	Zn-Pb-Ag	Vertical pipe-like	NW-trending thrust faults	Massive, disseminated, brecciated and bands	Ore minerals: sphalerite, galena and pyrite; gangue minerals: dolomite, calcite and quartz	Th:165–229 °C; sal:11.3–14.5 wt% NaCl eqv.	200.9	Zhang et al., 2014;
Southwestern Sichuan										
Daliangzi	Late Ediacaran Dengying Fm. dolostone	> 1.8 Mt, 10–12 wt%	Zn-Pb-Ag-Ge-Ga-Cd	Vertical pipe-like	NW-trending thrust faults	Massive, disseminated	Ore minerals: sphalerite, galena and pyrite; gangue minerals: dolomite, calcite	Th:170–225 °C; sal:18.0 wt% NaCl eqv.	204.4	Zhang et al., 2015;
Tianbaoshan	Late Ediacaran Dengying Fm. dolostone	2.6 Mt,10–15 wt%	Zn-Pb-Ag-Ge-Ga-Cd	Vertical pipe-like	NNE-trending thrust faults	Massive, disseminated, brecciated	Ore minerals: sphalerite, galena and pyrite, chalcopyrite; gangue minerals: dolomite, calcite	Th:157–167 °C; sal:12.4–20.0 wt% NaCl eqv.	>165	Zhang et al. 2015; Wang et al.,2012
Wusihe	Late Ediacaran Dengying Fm. dolostone	>3.7 Mt, 10.6–15.7 wt%	Zn-Pb-Ag	Stratabound and steeply dipping vein	NE-trending thrust fault	Massive, banded, brecciated and stock-work	Ore minerals: sphalerite, galena and pyrite; gangue minerals: quartz, dolomite, calcite and bitumen	Th:120–260 °C; sal:6.5–14.8 wt% NaCl eqv.	411	Xiong et al., 2018; Luo et al., 2020; Wei et al., 2020
Chipu	Late Ediacaran Dengying Fm. dolostone	0.65 Mt, 10.4 wt%	Zn-Pb-Ga-Cd-Ag	Stratabound and lenses	NNW-trending thrust-folds	Massive, disseminated, brecciated	Ore minerals: sphalerite, galena and pyrite; gangue minerals: quartz, dolomite, calcite and bitumen	Th:130–250 °C; sal:8.5–17.0 wt% NaCl eqv.	>165	Wu et al., 2013

Note: Th = Homogenization temperature; salinity = sal.

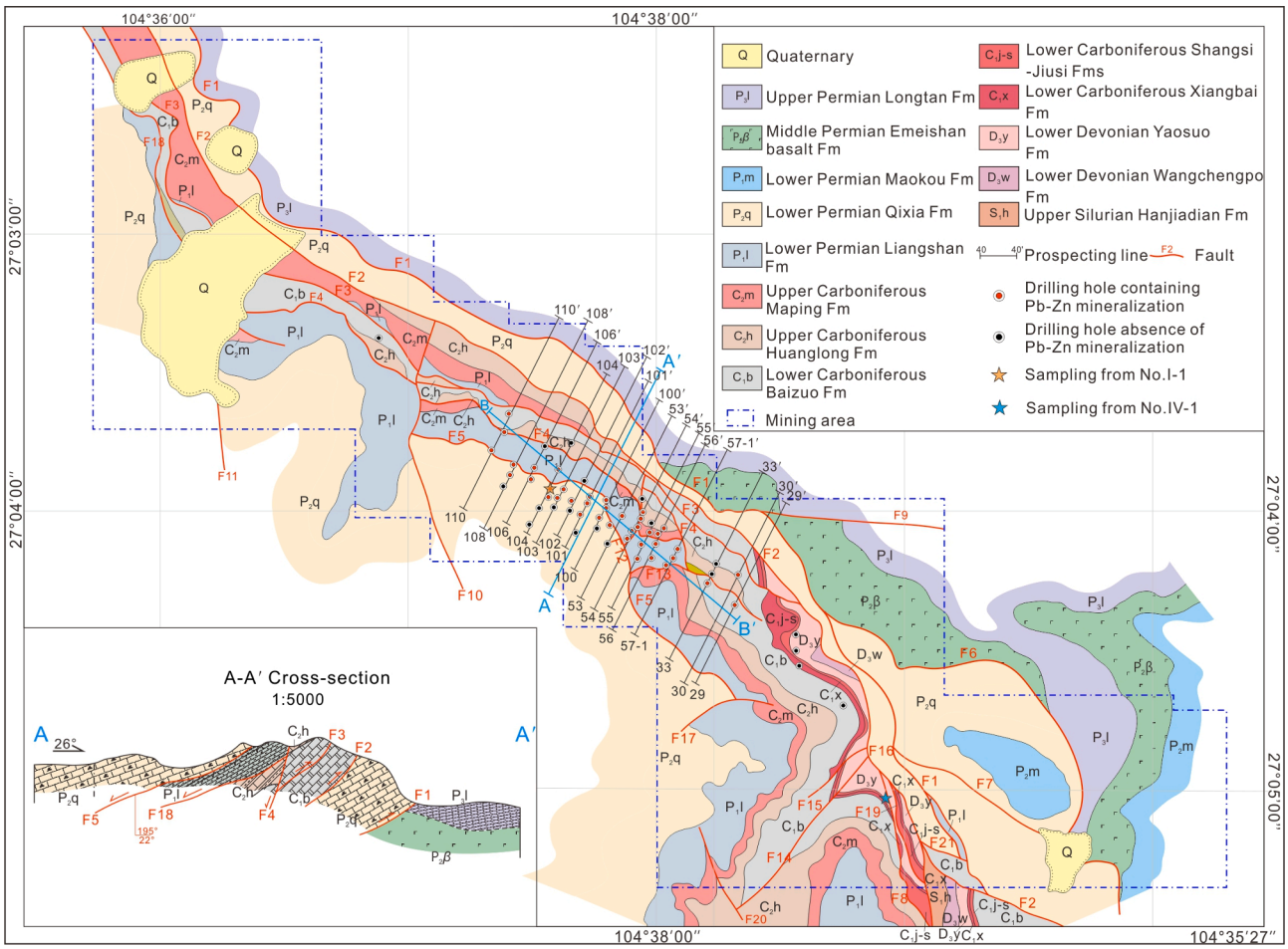

Fig. 2. Geological map of the Zhugongtang deposit showing stratigraphy and structure and the A-A' cross-section schematically displays the thrust system in the Zhugongtang mining area. Prospecting line 103-103′ and line 104-104′ and vertical section B-B' indicate the cross-sections shown in Fig. 4.

(average 11.0 m) thick with the grade of 0.09–37.01 wt% Zn and 0.12–10.14 wt% Pb, respectively (He et al., 2019).

3.4. Mineralogy textures, and paragenesis

The ores are mainly sulfides, with less amounts of oxides. The metallic minerals include mainly pyrite (Py), sphalerite (Sp), and galena (Gn) with minor smithsonite, cerusite and limonite, accompanied by hydrothermal dolomite (HD), calcite (Cal), quartz (Qtz), bitumen and potassium feldspar as the gangue minerals (Figs. 5 and 6). Hand specimen observations identified four types of sulfide ores in the Zhugongtang deposit, including massive, vein, disseminated and stock-work (Fig. 5).

Based on the mineral assemblage, texture and crosscutting relationship, three stages can be identified: diagenetic, hydrothermal and supergene phases, among which the hydrothermal stage can be further subdivided into three stages as: S1, early ore-stage (Qtz + Py + Sp); S2, main ore-stage (Sp + Gn + Py) and S3, late ore-stage (Cal + HD ± Gn). The detailed mineral paragenesis is shown in Fig. 7.

S1

The S1 stage is dominated by coarse-grained euhedral Py1 and subhedral Sp1 with minor irregular Gn1 and quartz (Fig. 6a–c). Py1 is the earliest hydrothermal sulfide in the entire hydrothermal mineralization process. It occurs as medium to coarse-grained (0.2–1 mm in diameter) and is commonly enclosed or partially replaced by Sp1 (Fig. 6a–g). Alternatively, Sp1 is subhedral coarse-grained (2–5 mm in diameter) and enclosed by later Gn2 (Fig. 6d) or enclosed by Py2 and Sp2 (Fig. 6f, g). Locally, fine-grained Gn1 inclusions distribute in the contact interfaces between Py1 and Sp1 (Fig. 6d). Quartz, the main gangue mineral of this stage, occurs as the euhedral fine-grained (0.1–0.3 mm in diameter) and is enclosed by later formed Gn2 (Fig. 6e).

S2

The S2 predominantly consists of coarsely crystallized Sp2, Gn2, fine-grained Py2 aggregates and minor potassium feldspar, bitumen, and Cal1 (Fig. 6e–m). Sp2 is commonly enclosed by later Gn2 (Fig. 6e, m) and/or crosscut by Gn2 (Fig. 6h). In some cases, the color zoned Sp2 overgrows with the dark Sp1 and Py1 (Fig. 6g). Gn2, coarse-grained (1–3 mm in diameter), encloses the early Sp2 (Fig. 6e) and overgrows with Sp2 (Fig. 6d, k, m). Locally, Gn2 fills the vug/grain interfaces of early Py1 or Py2 (Fig. 6a, i, j). Bitumen is commonly observed in this stage and enclosed by Gn2 (Fig. 6e, k) or overgrowing with Gn2 (Fig. 6j). Locally, the potassium feldspar is enclosed by Gn2 (Fig. 6j).

S3

In the S3 stage, vug filling gauge minerals formed such as calcite and hydrothermal dolomite, marking the final stage in the paragenesis (Fig. 6b–c, g, k–m). These minerals are subhedral to euhedral and commonly overgrow with the sulfides (Fig. 6k–m) fill in the residual porosity of the early formed sulfides (Fig. 6f). Locally, sparse Gn3 occurs as fine-grained and randomly distributes in the vug of the calcite (Fig. 6e).

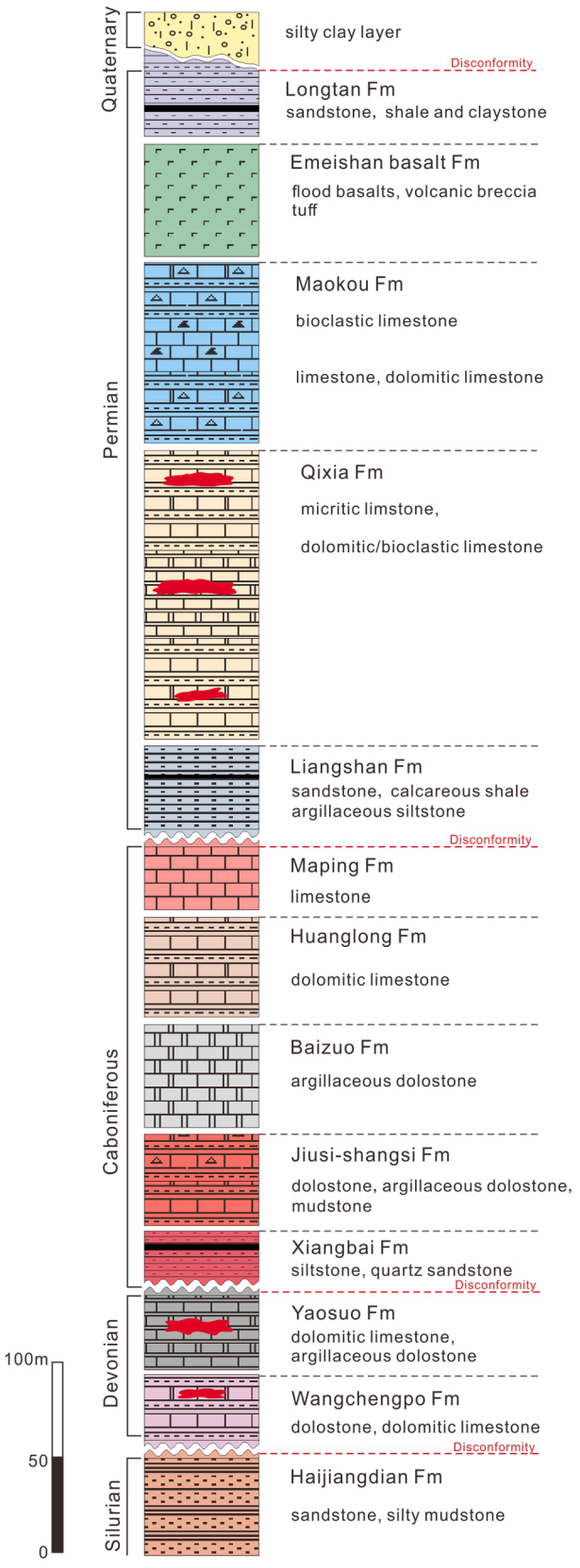

Fig. 3. The stratigraphic column of the Zhugongtang mining area showing the lithologies and locations of Zn-Pb orebodies.

Hydrothermal alteration

Hydrothermal alterations were developed in the country rock. Associated mineral assemblages in the host rocks include dolomite, calcite, pyrite, bitumen and quartz (Fig. 5c–f, h, j, k), of which calcite- and dolomite-altered zones are the most common. Calcite is widely distributed in the host rock which shows a close spatial relationship with the Zn-Pb mineralization (Fig. 5d–f, h, k). In some cases, pyrite shows intimate association with the ore grade of sulfide ores (Fig. 5c, d).

4. Sampling and analytical methods

4.1. Sampling

Thirty-seven samples from different orebodies and mining levels were chosen for in-situ compositional and isotopic analyses. These sulfide samples were collected from the underground mining tunnels (orebody IV-1) and ZK10405 drill core (orebody I-1; Fig. 4c). Thirty-one calcite were handpicked from sulfide samples by micro-drill and binocular microscope for C-O analysis. Five and twelve polished thin sections were selected for in-situ trace elements and S-Pb isotopes analysis, respectively. In situ Pb isotopic composition of sphalerite and pyrite was not determined, because their high Hg content could significantly affect the quality of the obtained Pb isotopic data.

4.2. Analytical methods

4.2.1. LA-ICPMS multi-element analysis

SEM images were obtained using a JSM-6460lv (JEOL, Japan) SEM equipped with a TEAM Apex XL (EDAX, America) EDS at the State Key Laboratory of Ore Deposit Geochemistry (SKLODG), Institute of Geochemistry, Chinese Academy of Science (IGCAS). An acceleration voltage of 20 kV, a probe current of ~10 nA, and a magnification of 200 × were used for most images.

Trace element analysis in pyrite was conducted by LA-ICPMS at the SKLODG, IGCAS, using a RESOLution-LR-S155 laser microprobe equipped with a Coherent Compex-Pro 193 nm ArF excimer laser coupled to an Agilent 7700x ICPMS instrument. Helium (350 ml/min) was applied as a carrier gas. A total of 41 spots were selected on five samples covering two generations of pyrite. The ablated aerosol was mixed with Ar (900 ml/min) before exiting the cell. Each analysis includes 30 s laser-off background measurement and 60 s laser-on sample analysis. Analyses were run with 26 μm spot size, 5 Hz pulse frequency and 3 J/cm^2 fluence. The following isotopes were monitored: ^{25}Mg, ^{27}Al, ^{29}Si, ^{34}S, ^{39}K, ^{43}Ca, ^{45}Sc, ^{49}Ti, ^{51}V, ^{53}Cr, ^{55}Mn, ^{57}Fe, ^{59}Co, ^{60}Ni, ^{65}Cu, ^{66}Zn, ^{71}Ga, ^{74}Ge, ^{75}As, ^{77}Se, ^{85}Rb, ^{88}Sr, ^{95}Mo, ^{107}Ag, ^{111}Cd, ^{115}In, ^{118}Sn, ^{121}Sb, ^{125}Te, ^{138}Ba, ^{184}W, ^{205}Tl, ^{208}Pb and ^{209}Bi. Pyrite was assumed to be stoichiometric and processed using an internal standard of 46.5 wt% Fe. Calculation standard STDGL2b3 was used to determine concentrations of chalcophile and siderophile elements (Danyushevsky et al., 2011). The integrated count data to concentrations for lithophile elements were calibrated and converted by GSE-1G and GSD-1G (USGS). The complete trace element dataset for each element in each sample are shown in Table S1.

4.2.2. Bulk C-O isotope analysis

Bulk C-O isotope analysis was conducted at the SKLODG, IGCAS, using a Finnigan MAT-253 gas isotope ratio mass spectrometer. The analytical procedures are as follows (i) calcite samples were reacted with 100% phosphoric acid (for 24 h at 72°C) to release CO_2, and (ii) the collected CO_2 was transferred to the mass spectrometer for the C-O isotopes analysis. $\delta^{13}C$ calculation was performed with the international standard V-PDB, whilst that of $\delta^{18}O$ used the international standard PDB and SMOW. The analytical precision calculated from replicate analyses of unknown samples was ± 0.05‰ for $\delta^{13}C$ and ± 0.08‰ for $\delta^{18}O$. $\delta^{18}O_{V\text{-}SMOW} = 1.03086 \times \delta^{18}O_{V\text{-}PDB} + 30.86$ (Friedman and O'Neil,

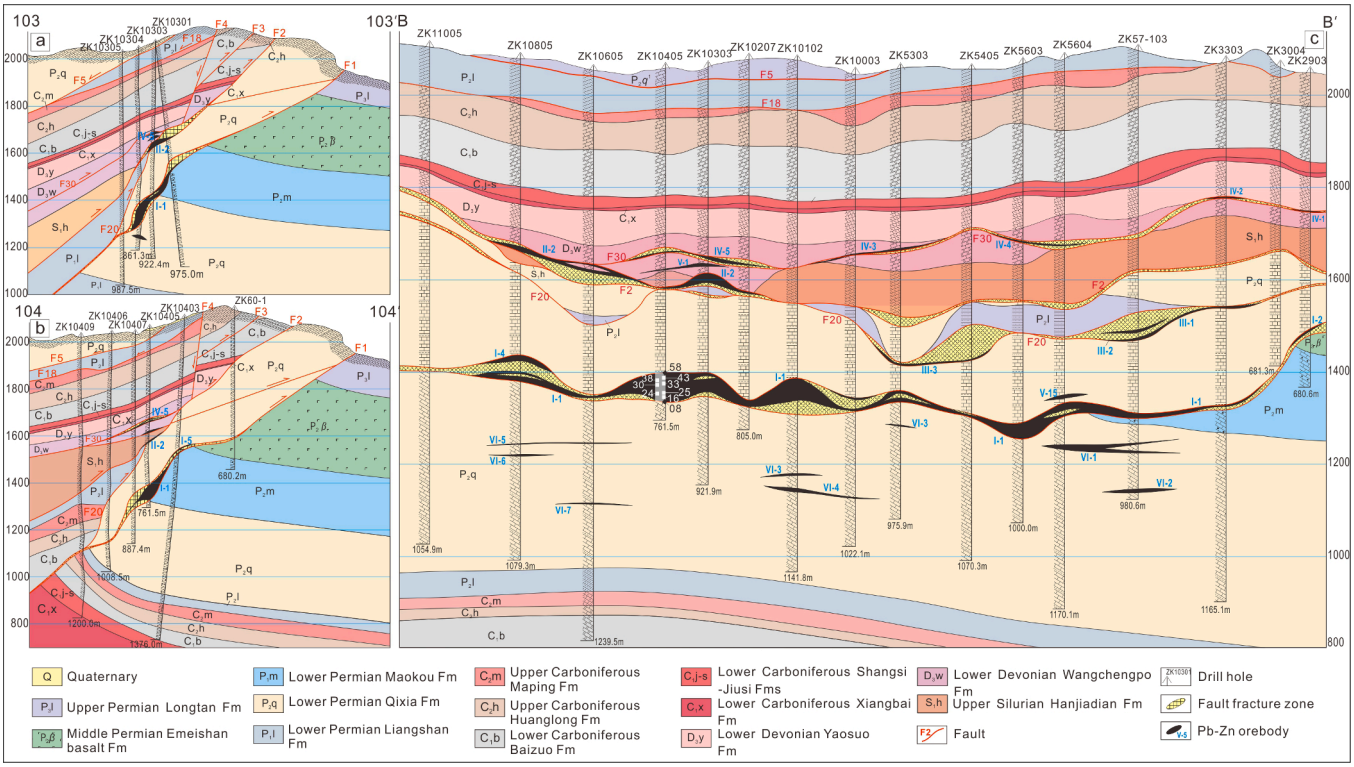

Fig. 4. Cross-sections through the Zhugongtang deposit, showing the thrust system, spatial relationship among different strata units, and orebodies (modified after Guizhou Dingshengxin Mining Development Co. Ltd unpub. result). Representative cross-sections along prospecting (a) line 103-103′, (b) line 104-104′, (c) vertical section B-B'. The locations of the cross-sections are indicated in Fig. 2.

1977).

4.2.3. LA-MC-ICPMS S and Pb isotope analyses

In-situ S isotope analyses were conducted on a Nu-Plasma 1700 MC-ICPMS (Nu Instruments, United Kingdom) that was attached to a RESOlution-155 ArF193-nm laser ablation system (Australian Scientific Instruments) at the State Key Laboratory of Continental Dynamics (SKLCD), Northwest University, China. Detailed description of the measuring procedures is available in Chen et al. (2017). Sixty-three micro-scale S isotopes covering different ore-stages were performed on 11 sulfide samples. These sulfides were ablated at a spot size of 30 μm, using a fluence of 3.6 J/cm^2 at 3 Hz. Under these conditions, 80 s analysis time (including a 30 s background collection and 50 s of ablation signal collection) for each sample is needed to obtain an internal precision of $^{34}S/^{32}S \leq \pm 0.000002$ (1σ). Instrument drift and mass bias were corrected using a sample standard bracketing (SSB) approach with repeated measurement of the standard before and after each sample. The international standard, NBS123 (sphalerite) and in-house standards Py-4 (pyrite) and CBI-3 (galena) were used for calibration in the sulfur isotope analyses. The analytical precision calculated from replicate analyses of unknown samples is better than 0.2‰ (1σ). The measured $\delta^{34}S_{CDT}$ (‰) of 17.8 ± 0.5‰ (2σ, $n = 156$) for standard NBS123 agrees well with that of reported value of 17.8 ± 0.2‰ (Chen et al., 2017).

In-situ Pb isotope analyses were performed on a Neptune Plus MC-ICPMS (Thermo Fisher Scientific, Germany) equipped with a Geolas HD excimer ArF laser ablation system (Coherent, Germany) at the Wuhan Sample Solution Analytical Technology Co. Ltd, China. Thirty-five in-situ Pb isotopes were carried out on seven galena samples. These samples were ablated with a spot size of 10 μm with a laser ablation frequency of 5 J/cm^2 at 8 Hz. Each sample acquisition consisted of 30 s background measurement time followed by 50 s of ablation for signal collection and an additional 40 s of wash time to reduce memory effects. The mass fractionation of Pb isotopes was corrected by $^{205}Tl/^{203}Tl$ with the exponential law. The optimized values of $^{205}Tl/^{203}Tl$ were calibrated from measuring two sulfide standards MASS-1 (USGS) and Sph-HYLM (sphalerite, in-house standard), replaced the natural Tl isotopic composition for the mass fractionation correction of Pb isotopes. The ^{202}Hg signal was used to correct the remaining ^{204}Hg interference on ^{204}Pb, using the natural $^{202}Hg/^{204}Hg$ ratio (0.2301). Sph-HYLM was used to monitor the precision and accuracy of the measurements after ten sample analyses, over the entire period of analysis. The obtained accuracy is better than ± 0.2‰ for $^{208}Pb/^{204}Pb$, $^{207}Pb/^{204}Pb$ and $^{206}Pb/^{204}Pb$ compared to the solution value by MC-ICPMS with a typical precision of 0.4‰ (2σ). More detail of the in-situ Pb isotopic ratios analysis was described in Zhang et al. (2016).

5. Results

5.1. Trace elements in pyrite

Trace element concentrations of two stages pyrite (Py1–Py2) are listed in Table S1 and representative trace elements are listed in Table 2. The concentrations of V, Cr, Mn, Ni, Cu, Zn, As, Ag, Sb, Tl and Pb are above minimum detection limit in the majority of pyrite grains whilst Co, Se, Mo, In and Bi concentrations are detected in some pyrite grains. Except that Pb content show highly variable, other elements show relatively uniform concentrations (Table 2 and Fig. 8). Specifically, arsenic is the most abundant trace element in pyrite with a median value of 4449 ppm in Py1 and 2288 ppm in Py2. As the important economic elements in the Zhugongtang deposit, Pb and Zn are significantly enriched in Py1 with the median value of 2009 ppm and 321 ppm, respectively. Sliver, Sb and Tl are relatively enriched in Py1 with the median value of 21.7 ppm, 103 ppm and 0.92 ppm, respectively. In addition, all types of pyrite contain a small amount of V, Cr, Mn, Co, Ni, Cu, Se, Mo, In and Bi (Table S1).

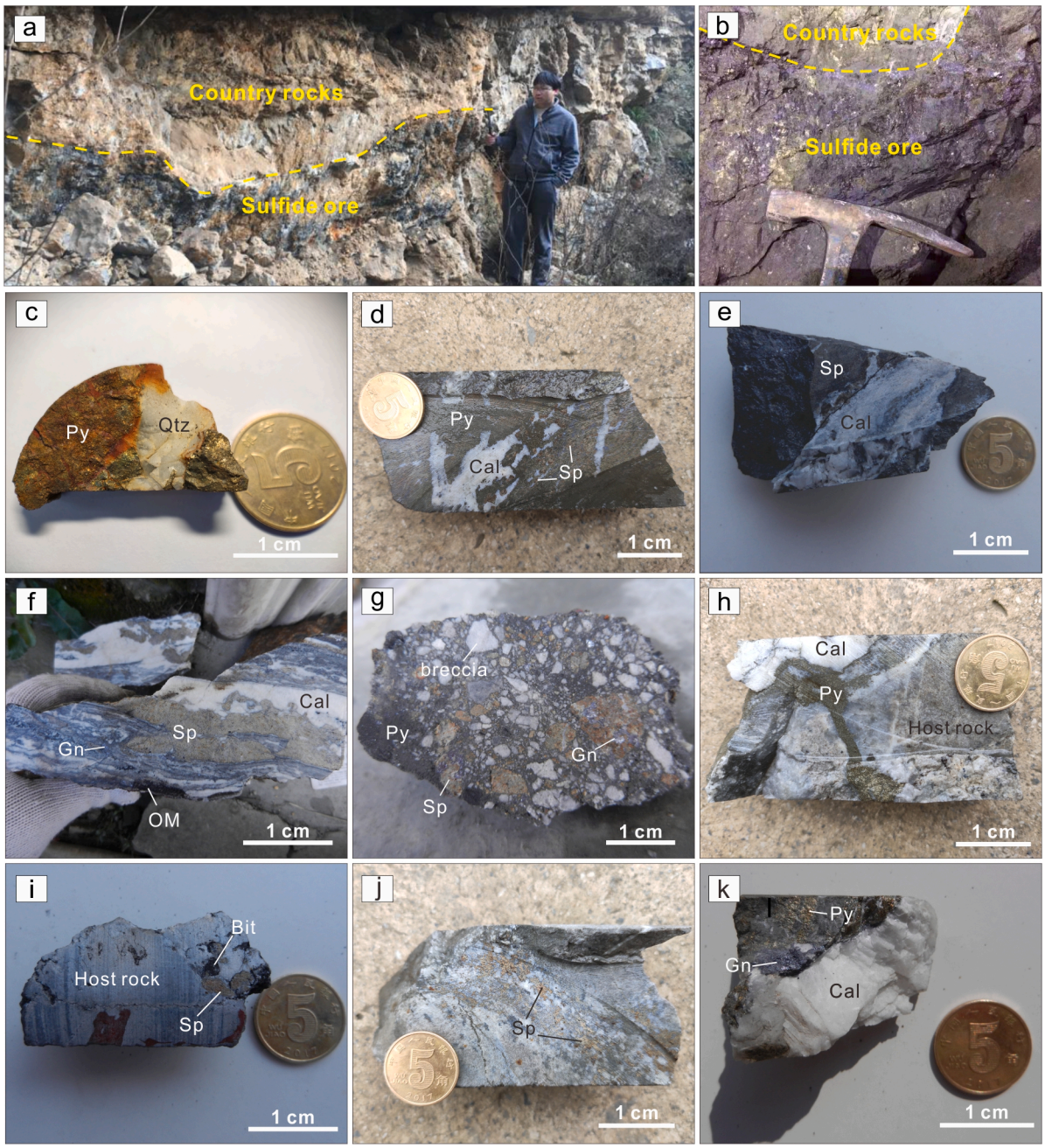

Fig. 5. Photographs showing the occurrences and ore textures of the Zhugongtang deposit. (a) Stratiform shape sulfide ores. (b) Irregular boundary between sulfide ores and country rocks. (c) Massive pyrite overgrows with quartz in hand specimen. (d) Massive sulfide ore. (e) Sphalerite ore crosscut by hydrothermal calcite vein. (f) Banded sulfide ores. (g) Sulfide ores cement the brecciated country rocks. (h) Pyrite vein filling the fracture of country rocks. (i) Sphalerite ore and bitumen in the vug of carbonate rocks. (j) Disseminated sphalerite occurring in the country rocks. (j) Post-ore calcite overgrowth with pyrite and galena. Abbreviation: Qtz = Quartz; Py = pyrite, Sp = sphalerite, Gn = galena, Bit = bitumen, HD = hydrothermal dolomite, Cal = calcite.

5.2. Bulk C-O isotopic compositions

The C and O isotope data for the calcite from Zhugongtang are listed in Table 3 and plotted in Fig. 9. Calcite from two ore-stages have $\delta^{13}C_{PDB}$ and $\delta^{18}O_{SMOW}$ values ranging from −7.53 to +1.73‰ and +13.85 to +21.88‰, respectively. The $\delta^{13}C_{PDB}$ values are between −7.53 to −1.65‰ for Cal1 from S2 and from −4.83 to +1.73‰ for Cal2 from S3, and the $\delta^{18}O_{SMOW}$ values are from +17.10 to +21.88‰ for Cal1 from S2 and +13.85 to +18.40‰ for Cal2 from S3.

5.3. In-situ S isotopic values

The analyzed sulfides (pyrite, sphalerite, and galena) span from both paragenesis and the vertical extent of the deposit (Table 4 and Fig. 10). The $\delta^{34}S$ values in sulfides display large ranges (+12.2 to +23.8‰) but with insignificant variation among different vertical levels. Two sulfide samples selected from the orebody IV-1 (hosted within Devonian strata) have the $\delta^{34}S$ values of +18.5 to +23.8‰ (n = 12), whilst nine samples from the orebody I-1 (hosted within Permian strata) have the $\delta^{34}S$ values of +12.2 to +15.3‰ (n = 51). In general, the $\delta^{34}S$ values of S2 sulfides display slightly higher $\delta^{34}S$ values than S3 sulfides (Table 4 and Fig. 10), for example, the $\delta^{34}S$ values of S1 sulfides (Py1 and Sp1) from the

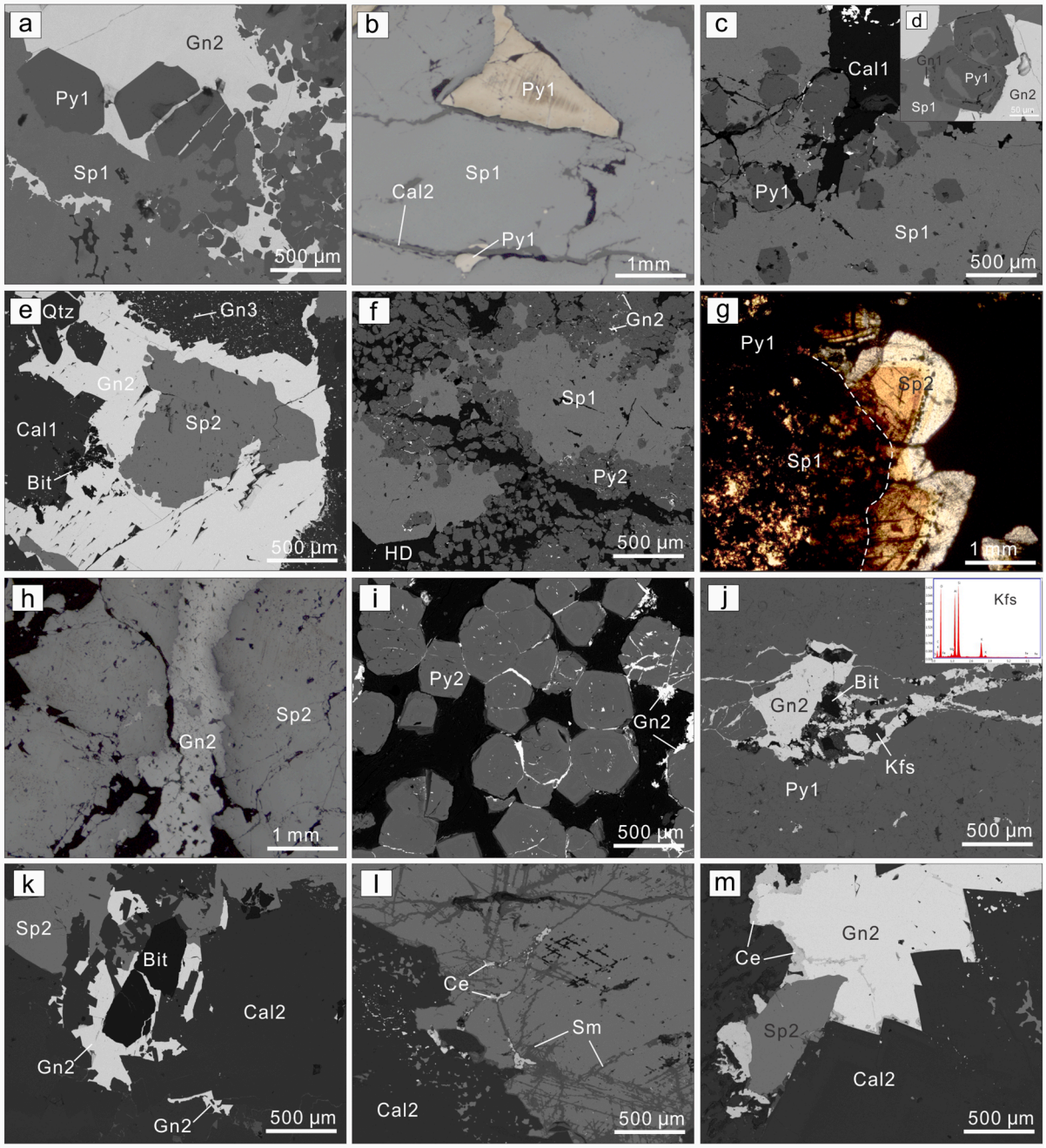

Fig. 6. Scanning electron microscopy (SEM) images (a, c-f, i-m) and photomicrographs of reflected-light (b, h) and transmitted-light (g) showing ore texture and mineral assemblages of sulfides. (a) Py1 is replaced by Sp1, and Gn2 filling in residual space. (b) Subeuhedral Py1 enclosed by later Sp1, which crosscut by Cal2. (c) Fine-grained pyrite enclosed/replaced by Sp1. (d) Euhedral Py1 aggregate is replaced by Sp1, both later enclosed by Gn2. (e) Quartz aggregate, nearly euhedral Sp2 and euhedral Cal1 enclosed by the later formed Gn2. (f) Py1 replaced by coarse-grained Sp1, which further enclosed by Py2 aggregates. (g) Dark Sp1 overgrows with the light Sp2. (h) Gn2 vein cross-cuts coarse-grained Sp2. (i) Gn2 veins cross-cut euhedral Py2 or filling in the voids of Py2 grain interfaces. (j) Gn2-bitumen-potassium feldspar filling in the vug of the Py1. (k) Gn2 and Sp2 filling pore space and enclosing Cal2 euhedral termini around the former void margins, and also enclosing Bitumen. (l) Smithsonite and cerusite distributes in the cracks of the sphalerite. (m) Sp2 overgrows with Gn2 that is oxidized along the crystal rim. Abbreviations: Kfs = Potassium feldspar, Sm = Smithsonite, Ce = Cerusite, other abbreviations are the same as in Fig. 5.

orebody IV-1 range from +22.56 to +23.8‰, and those of S2 sulfides (Sp2 and Gn2) range from +18.5 to +21.4‰.

5.4. In-situ Pb isotope ratios

In-situ Pb isotopic ratios were obtained for galena selected from different ore-bearing strata, mining levels (Table 5 and Fig. 11). Galena grains have the following in-situ Pb isotopic ratio: $^{206}Pb/^{204}Pb$ = 18.566–18.758, $^{207}Pb/^{204}Pb$ = 15.757–15.769 and $^{208}Pb/^{204}Pb$ = 39.061–39.366, with insignificant variation with respect to vertical location of the samples. In detail, galena from different paragenetic sequences shows variable Pb isotopic ratio. Subhedral Gn1 (coexisting with Sp1 and Py1) grains from the orebody IV-1 have $^{206}Pb/^{204}Pb$ ratios of 18.701–18.729, $^{207}Pb/^{204}Pb$ ratios of 15.761–15.768 and $^{208}Pb/^{204}Pb$ ratios of 39.109–39.319, which are slightly lower than those of anhedral Gn2 ($^{206}Pb/^{204}Pb$ = 18.738–18.758, $^{207}Pb/^{204}Pb$ = 15.766–15.769 and $^{208}Pb/^{204}Pb$ = 39.279–39.366).

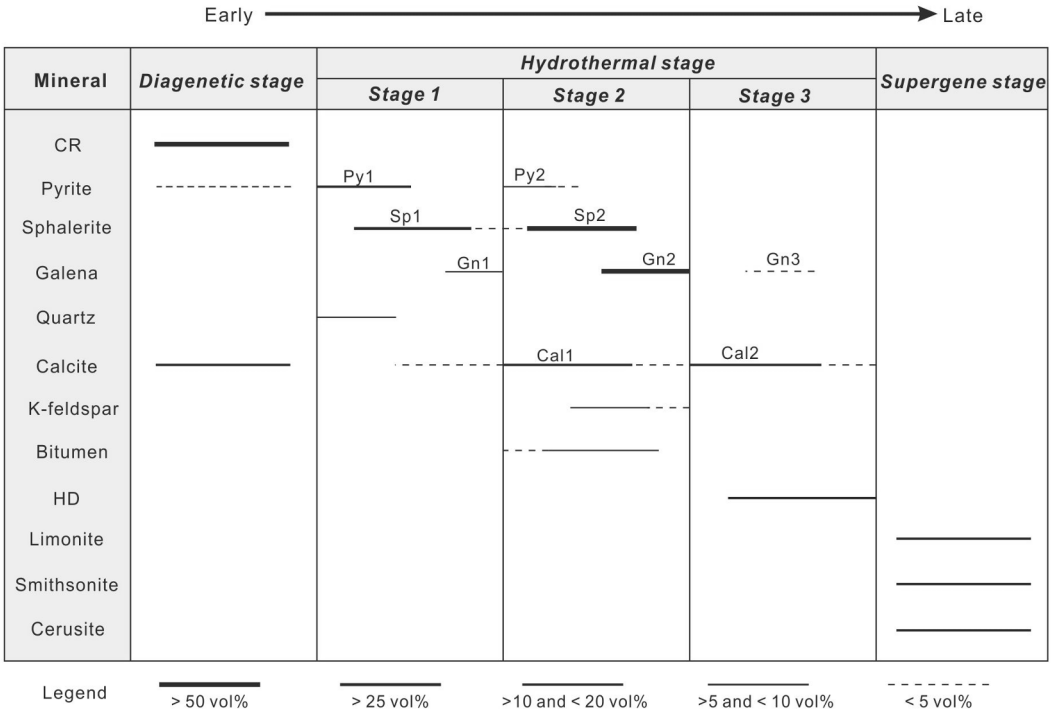

Fig. 7. Mineral paragenetic sequence for the Zhugongtang deposit. Abbreviations: CR = carbonate rocks, other abbreviations are the same as in Fig. 5.

6. Discussion

6.1. The nature of hydrothermal fluid

6.1.1. Trace elements in pyrite as an indicator of physicochemical conditions

The geochemical behavior of trace elements in the hydrothermal system is controlled by the physicochemical conditions of fluid (e.g., Hannington et al., 1995; Maslennikov et al., 2009). This information could be recorded by the variable composition in pyrite from different generations. Therefore, the trace element distributions in pyrite could reflect the environment (e.g., *T*, fO_2 and pH) of hydrothermal fluid during the sulfide precipitation.

The *T*-sensitive elements (e.g., As, Zn, Sb and Pb) are commonly enriched in sulfide deposits under low-temperature conditions (Maslennikov et al., 2009). In the Zhugongtang deposit, the contents of As, Zn, Sb and Pb are the highest in all pyrite types, indicating low-temperature conditions for the formation of pyrite. The Co/Ni ratio of pyrite can also be used as a temperature indicator. Co/Ni < 1 usually suggests a low-temperature hydrothermal condition, while Co/Ni > 1 represents a high-temperature ore-forming environment (Bralia et al. 1979; Maslennikov et al. 2009; Maghfouri et al., 2018). The studied pyrite grains have relatively low Co (mainly < 1.0 ppm) and Ni (<10.0 ppm) with the Co/Ni ratios of <0.01–0.20 (Fig. 12a) together with pyrite co-existing with sphalerite and galena (Figs. 5 and 6), suggesting the Zn-Pb mineralization at Zhugongtang was formed at a low-temperature condition, which further is supported Tl content in pyrite. Tl content in pyrite varies from < 0.03 to 22.8 ppm (Fig. 12b), comparable to the Tl content (0.001–100 ppm) in pyrite deposited between 100 and 250 °C under weakly reduced conditions (e.g., Hannington et al., 1995). Additionally, the well-developed solution collapse and replacement textures at Zhugongtang together with abundant pyrite in ore-stages likely indicate the hydrothermal fluid is acidic, as supported by unaltered K-feldspar observed in calcite veinlet. The K-feldspar grains (which overgrows with galena, Fig. 6j) would be altered into the sericite (muscovite) and kaolinite if the hydrothermal fluid had pH values < ~5–5.5 at 200 °C (Rusk et al., 2008). However, extensive SEM examination did not reveal that any evidence for the alteration of K-feldspar. Therefore, the sulfides in the Zhugongtang deposit were precipitated from a low-temperature (100–250 °C), low fO_2 and weakly acidic (pH > 5.5) hydrothermal fluid.

6.1.2. Sources of carbon and origin of ore-forming fluid

Hydrothermal fluids in different reservoirs display distinct C-O isotope compositions: (1) mantle ($\delta^{13}C_{PDB} = -8$ to -4‰ and $\delta^{18}O_{SMOW} = +6$ to $+10$‰; Taylor et al., 1967), sedimentary organic matter ($\delta^{13}C_{PDB} = -30$ to -15‰ and $\delta^{18}O_{SMOW} = +24$ to $+30$‰; Hoefs 2009) and marine carbonate rocks ($\delta^{13}C_{PDB} = -4$ to $+4$‰ and $\delta^{18}O_{SMOW} = +20$ to $+30$‰; Veizer and Hoefs, 1976). In the $\delta^{13}C_{PDB}$ vs. $\delta^{18}O_{SMOW}$ diagram (Fig. 9a), data for Cal1 and Cal2 have variable C ($\delta^{13}C_{PDB} = -7.53$ to $+1.73$‰), falling on the evolution line of the carbonate dissolution in the area adjacent to the marine carbonate rock, with some of the calcite samples trending toward the dehydrogenation the baseline of the sedimentary organic matter (Fig. 9b), indicating that the hydrothermal calcite was mainly formed by dissolution and/or recrystallized of the host rock (limestone) with a contribution from the organic carbon as suggested by the roughly negative correlation (r = 0.68) between $\delta^{13}C_{PDB}$ and $\delta^{18}O_{SMOW}$ (Fig. 9b). The data suggest that mixing of two C sources during ore-forming process caused the crystallization of the hydrothermal calcite.

The $\delta^{18}O_{SMOW}$ values of hydrothermal calcite display a general downward trend from Cal1 (+17.10 to +21.88‰) to Cal2 (+13.85 to +18.40‰). A similar trend has been reported from other carbonate-hosted deposits (such as Nayongzhi, Maoping; Wei, 2018; He et al., 2020) in the SYMP where lighter O isotope composition is observed in paragenetically late carbonate minerals. Lighter $\delta^{18}O$ isotope value of Cal2 relative to Cal1 may be attributed to either increase in mineralizing temperature or the introduction of $\delta^{18}O$-depleted hydrothermal fluid (e.g., Ohmoto, 1986). The latter hypothesis is favored by the reason that the mineralizing temperature generally decreases from early to late ore-stage as suggested by fluid inclusion microthermometry (Guizhou Dingshengxin Mining Development Co. Ltd unpub. result). Using the average homogenization temperature of fluid inclusion at S2 (210℃) and S3 (175℃), the $\delta^{18}O_{SMOW}$ value of Cal2 and Cal3 and the oxygen

Table 2
Selected trace elements in different generations (Py1–Py2) of pyrite from the Zhugongtang deposit.

Sample no.	Analysis no.	Stage	V	Cr	Mn	Co	Ni	Cu	Zn	As	Se	Mo	Ag	In	Sb	Tl	Pb	Bi
ZK10405-14	spot 1	S2	0.22	70.6	9.77	<0.14	3.78	14.0	6.33	6690	10.1	0.12	7.50	<0.02	299	1.21	2486	<0.05
	spot 2	S1	0.25	18.3	43.2	<0.21	<0.82	16.4	250	239	<12.5	<0.14	4.28	<0.01	4.72	0.14	412	<0.06
	spot 3	S2	0.15	22.5	<0.62	0.08	<0.36	31.1	5.52	2078	5.95	0.03	19.9	<0.01	106	0.65	885	<0.02
	spot 4	S2	0.05	5.31	1.40	<0.07	<0.53	8.38	<1.46	1390	<4.86	0.04	10.4	<0.01	38.0	<0.06	175	<0.03
	spot 5	S2	<0.11	14.2	3.28	<0.11	<0.95	68.4	<1.84	4365	11.1	0.13	12.0	<0.02	71.1	0.40	1010	<0.05
	spot 6	S1	0.20	40.0	1.35	<0.07	<0.97	3.34	318	2297	<10.7	<0.16	<2.18	<0.02	32.8	<0.11	197	<0.05
	spot 7	S2	0.17	21.6	<0.61	0.03	0.30	54.4	1.45	1504	6.71	<0.06	13.1	<0.004	472	0.22	2031	<0.02
	spot 8	S2	0.08	28.4	<0.63	<0.05	<0.33	61.1	<2.00	4519	<4.1	<0.02	70.4	<0.01	585	0.36	3885	<0.02
ZK10405-25	spot 1	S2	0.14	3.81	1.65	<0.12	<1.02	11.7	<2.30	401	<9.13	0.05	5.89	<0.01	308	0.07	1382	<0.05
	spot 2	S2	0.09	5.93	<0.46	<0.05	0.34	70.6	1.36	492	5.42	0.02	5.44	0.01	545	0.12	1652	0.03
	spot 3	S1	0.74	7.21	1.68	0.41	3.01	35.5	340	10,162	<6.66	0.27	9.18	0.01	344	0.11	2832	<0.04
	spot 4	S2	<0.05	4.13	2.78	0.10	0.86	15.2	<1.92	7585	<5.72	0.05	3.85	<0.002	24.1	<0.12	454	<0.04
	spot 5	S1	0.22	28.4	0.86	0.22	1.48	43.3	80.3	3950	4.32	0.06	17.0	0.00	445	0.17	2438	<0.02
	spot 6	S1	0.05	5.00	1.03	0.53	4.40	7.37	325	3221	<5.52	<0.35	<2.11	0.01	54.1	0.08	790	<0.04
	spot 7	S2	0.03	6.57	0.48	<0.01	<0.16	16.4	<1.30	6221	<2.11	<0.02	2.52	<0.01	103	0.02	1538	<0.02
	spot 8	S2	0.43	2.63	<0.40	<0.04	0.27	8.32	<0.99	209	<2.64	<0.01	6.77	<0.01	395	0.08	1388	0.03
ZK10405-41-1	spot 1	S2	1.81	59.9	1.20	0.07	21.1	101	6.45	25,812	5.37	0.86	69.7	0.02	77.8	2.47	3747	<0.02
	spot 2	S2	1.00	51.9	1.89	<0.13	14.6	125	6.82	23,390	<9.69	1.21	50.9	0.05	95.3	1.88	3394	<0.04
	spot 3	S2	0.41	7.94	<1.17	<0.12	<0.86	10.8	2.85	1850	<6.27	0.26	6.35	<0.002	389	0.26	1600	<0.04
	spot 4	S1	1.29	283	4.04	0.06	54.8	114	29,413	23,598	113	1.56	321	0.12	4516	22.8	299,103	0.05
	spot 5	S2	0.36	28.1	1.54	0.09	10.1	51.2	6.19	21,315	<4.03	0.30	38.4	0.00	127	1.25	3666	<0.02
	spot 6	S2	<0.04	1.19	<0.61	0.12	1.23	28.3	1.84	10,767	<6.29	0.18	<1.01	0.00	13.3	<0.03	19.6	0.03
	spot 7	S2	1.10	6.65	5.10	0.06	1.01	17.2	2.13	69.2	<4.88	0.14	6.33	0.01	378	0.17	888	<0.02
	spot 8	S2	0.11	5.09	<0.65	<0.06	1.25	1.66	2.04	2252	11.8	0.17	<1.263	0.02	3.94	0.03	6.26	0.02
ZK10405-30	spot 1	S2	0.04	27.1	6.98	<0.09	0.79	27.4	1.90	10,796	6.16	0.03	<1.88	<0.01	18.5	0.17	150	<0.03
	spot 2	S1	0.15	55.6	2.52	<0.09	4.11	55.9	46.1	16,496	<7.20	<0.01	12.8	0.01	45.2	1.33	1275	<0.03
	spot 3	S1	0.38	122	18.7	0.38	1.96	64.2	28,549	4948	<6.16	0.03	26.5	0.09	102	2.21	2357	<0.02
	spot 4	S1	0.69	67.4	8.72	0.42	10.4	73.6	14,364	5624	18.3	0.10	30.8	0.06	115	1.48	1662	<0.04
	spot 5	S1	0.51	125	5.09	0.81	7.23	34.3	80.5	2098	150	0.07	76.3	0.02	332	0.88	229,193	0.09
	spot 6	S1	1.31	38.2	10.4	0.28	4.20	20.7	2126	1588	<7.90	<0.03	14.1	0.01	73.6	0.92	1656	<0.03
	spot 7	S1	0.17	86.4	4.15	0.41	3.34	64.3	35.1	16,398	5.25	<0.03	29.4	0.01	104	4.82	4881	<0.02
	spot 8	S2	0.32	31.8	18.5	0.47	10.1	30.7	4.78	4040	11.6	0.03	25.5	0.00	83.0	1.52	17,794	0.05
ZK10405-8	spot 1	S2	0.84	6.67	0.82	<0.07	<0.47	97.9	2.52	9911	7.93	<0.01	9.02	0.01	561	0.34	3215	<0.02
	spot 2	S2	0.12	<2.41	<0.92	<0.11	1.91	2.18	<2.40	3061	4.96	<0.03	<1.70	0.02	30.3	<0.06	600	<0.03
	spot 3	S2	0.05	<2.07	<1.07	<0.07	<0.74	0.85	<2.41	2254	<5.99	<0.15	<1.70	<0.004	11.9	<0.04	214	0.06
	spot 4	S2	0.34	15.0	1.04	<0.11	<0.96	15.5	5.48	304	<8.97	<0.10	3.67	0.03	3.65	0.15	75.5	<0.03
	spot 5	S2	<0.05	3.37	<1.11	<0.12	<1.33	1.74	7.85	2288	<11.3	<0.23	<2.82	<0.02	1.74	0.07	37.4	<0.04
	spot 6	S2	0.09	4.31	<0.75	0.08	<0.77	15.0	<1.54	1968	<4.69	<0.07	6.19	<0.01	101	0.39	1050	<0.02
	spot 7	S2	0.19	20.2	<0.78	0.14	0.91	10.4	11.7	1174	12.5	<0.07	4.21	<0.02	63.2	0.89	488	<0.02
	spot 8	S2	<0.05	18.9	<0.58	<0.03	<0.42	18.6	<1.43	5925	<4.11	<0.05	<1.04	<0.01	1.84	0.05	3.98	0.02
	spot 9	S2	<0.08	4.12	<0.87	0.09	<0.64	40.0	2.31	90.3	<5.58	<0.04	4.64	<0.01	264	<0.06	857	<0.03

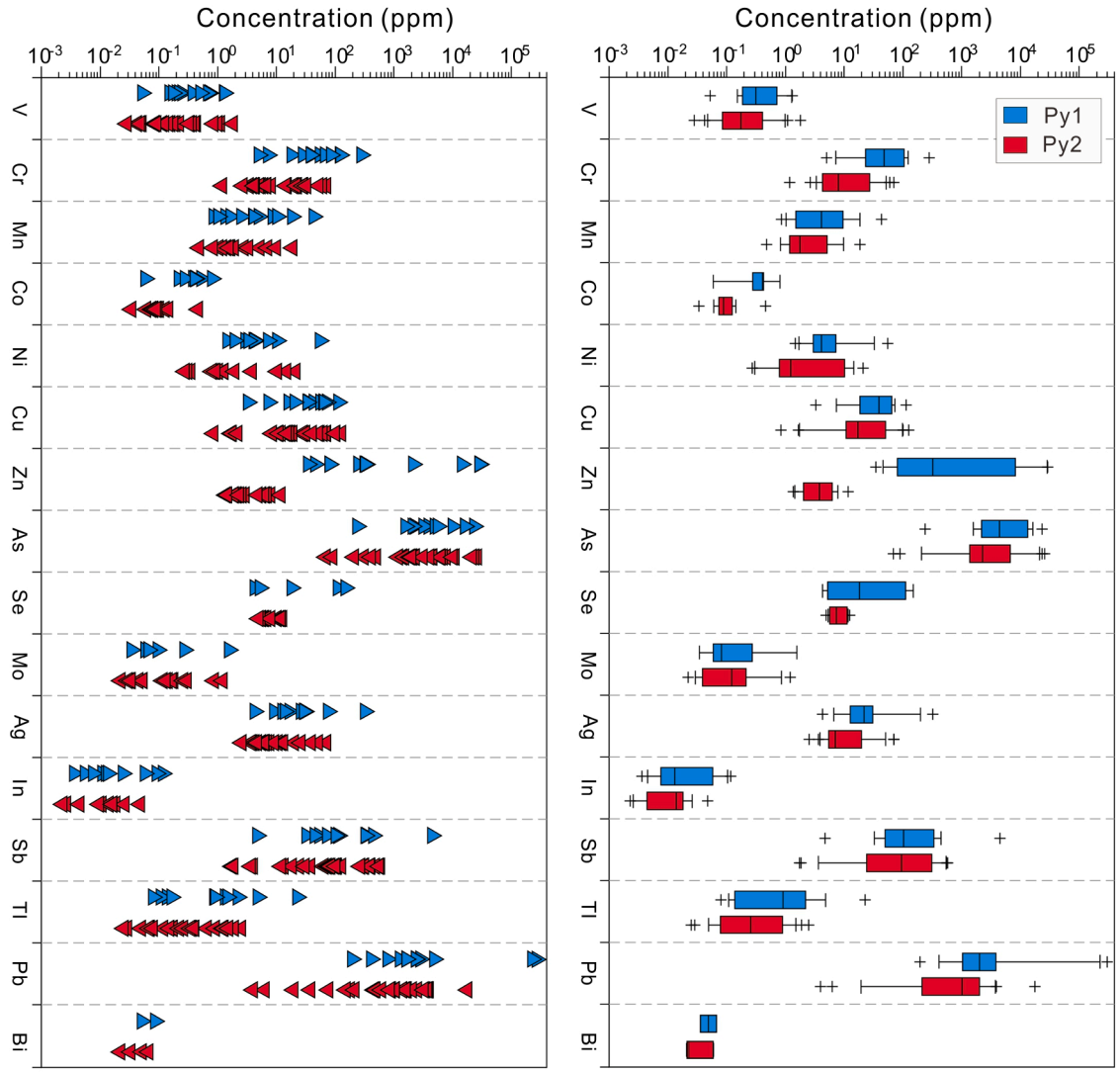

Fig. 8. LA-ICPMS data for selected trace elements of different generations (Py1–Py2) of pyrite from the Zhugongtang deposit. (a) Individual analyses. (b) Box and whisker plots.

isotope fraction equation: Friedman and O'Neil (1977), the calculated $\delta^{18}O$ of the fluid ranged from 8.58 to 13.36‰ at S2 and 3.40 to 7.95‰ at S3. The values lie between the basinal brines of the MVT ore deposits ($\delta^{18}O$ of +4.0 to +10.0‰; McLimans, 1977) and marine carbonate rocks ($\delta^{18}O_{SMOW}$ = +20 to +30‰; Veizer and Hoefs, 1976).

Overall, the carbon was sourced from the surrounding limestone with the involvement of a portion of organic matter, while O is derived through a mixing of the $\delta^{18}O$-depleted basinal brine and the $\delta^{18}O$-enriched limestone.

6.2. Constraints on the sources of reduced sulfur and metallic elements

6.2.1. Evidence from in-situ S isotopic composition

The S isotopic composition of sulfides and sulfate could not represent the total S isotope composition ($\delta^{34}S_{\sum S}$) of hydrothermal fluid due to the effect of *T*, fO_2 and pH (Ohmoto and Rye, 1979). The source of sulfur in the Zhugongtang deposit should be determined based on the $\delta^{34}S_{\sum S}$ of hydrothermal fluid during ore formation. As the hydrothermal fluids are dominated by H_2S with the environment of low fO_2 and pH value, the equilibrium state ($\delta^{34}S_{\sum S} \approx \delta^{34}S_{H2S} \approx \delta^{34}S_{pyrite}$) would be established (Zheng and Chen, 2000). The sulfide assemblage at Zhugongtang is dominated by pyrite, sphalerite, and galena in the absence of any sulfate minerals (e.g., gypsum and barite). Therefore, the H_2S is dominated in the S1–3 hydrothermal fluid and the sulfides were formed in relatively low fO_2 and pH conditions. The generally decreasing $\delta^{34}S$ values of sulfides at Zhugongtang ($\delta^{34}S_{pyrite} > \delta^{34}S_{sphalerite} > \delta^{34}S_{galena}$) can be comparable with the $\delta^{34}S$ enrichment condition of $\delta^{34}S_{pyrite} > \delta^{34}S_{sphalerite} > \delta^{34}S_{galena}$ at isotopic equilibrium, indicating the S isotope fractionation have reached equilibrium (Ohmoto and Rye, 1979). Therefore, the $\delta^{34}S$ values of the pyrite, sphalerite and galena can approximate represent the $\delta^{34}S_{\sum S}$ of hydrothermal fluid. The $\delta^{34}S$ values of sulfides range from +12.2 to +15.3‰ in orebody I-1 and from +18.5 to +23.8‰ in orebody IV-1, which are significantly higher than those of typical magmatic reservoir (0 ± 5‰, Ohmoto and Rye, 1979) but similar to the synchronic seawater sulfates and/or evaporitic sulfates in the ore-bearing strata of Permian (10.0–15.0‰, Claypool et al. 1980) and Devonian (18.0–24.0‰, Claypool et al. 1980; Ren et al. 2018), respectively. It indicates the reduced S (S^{2-}) in the S1–2 were completely converted from SO (the synchronic seawater sulfates and/or evaporitic sulfate) in a nearly closed system (e.g. Machel et al., 1995). The S^{2-} could be formed by either thermal-chemical sulfate reduction (TSR) or bacterial sulfate reduction (BSR). The former mechanism is favored by the following reasons: (i) the ore-forming temperature of the Zhugongtang deposit spans from 120 to 240 ℃ (Guizhou Dingshengxin Mining Development Co. Ltd unpub. result), higher than the survival temperature of sulfate-reducing bacteria (optimal 30 and 40 °C;

Table 3
. C-O isotopic composition of calcite in the Zhugongtang deposit.

Sample no.	Mineral	Stage	$\delta^{18}O_{PDB}$(‰)	$\delta^{18}O_{SMOW}$(‰)	$\delta^{13}C_{PDB}$(‰)	$\delta^{18}O_{fluid}$(‰)
ZGT- KB-1	Calcite	S1	−13.35	17.10	−1.65	8.58
ZK10405-1	Calcite	S1	−9.92	20.64	−3.95	12.12
ZK10405-2	Calcite	S1	−11.04	19.48	−4.13	10.96
ZK10405-6	Calcite	S1	−11.48	19.02	−4.19	10.50
ZK10405-12	Calcite	S1	−11.34	19.17	−4.38	10.65
ZK10405-14	Calcite	S1	−11.15	19.36	−4.20	10.84
ZK10405-15	Calcite	S1	−11.32	19.19	−3.82	10.67
ZK10405-16	Calcite	S1	−11.67	18.83	−4.63	10.31
ZK10405-19	Calcite	S1	−10.77	19.75	−6.07	11.24
ZK10405-26	Calcite	S1	−11.00	19.52	−4.27	11.00
ZK10405-28	Calcite	S1	−11.60	18.91	−4.73	10.39
ZK10405-30	Calcite	S1	−13.02	17.43	−4.44	8.92
ZK10405-31	Calcite	S1	−11.48	19.02	−3.77	10.50
ZK10405-35	Calcite	S1	−11.63	18.88	−3.63	10.36
ZK10405-41-2	Calcite	S1	−11.69	18.81	−3.88	10.29
ZK10405-42	Calcite	S1	−12.53	17.94	−3.89	9.42
ZK10405-43	Calcite	S1	−10.94	19.59	−4.06	11.07
ZK10405-45	Calcite	S1	−8.71	21.88	−7.53	13.36
ZGT-1	Calcite	S2	−15.39	14.99	1.73	4.54
ZK10405-11	Calcite	S2	−14.59	15.82	−3.87	5.37
ZK10405-13	Calcite	S2	−12.53	17.94	−3.62	7.49
ZK10405-18	Calcite	S2	−14.34	16.07	−3.00	5.62
ZK10405-22	Calcite	S2	−12.32	18.16	−4.28	7.70
ZK10405-23	Calcite	S2	−12.09	18.39	−4.43	7.94
ZK10405-32	Calcite	S2	−12.49	17.98	−3.44	7.53
ZK10405-33	Calcite	S2	−14.18	16.24	−3.28	5.79
ZK10405-36	Calcite	S2	−13.98	16.45	−4.83	6.00
ZK10405-37	Calcite	S2	−12.08	18.40	−3.93	7.95
ZK10405-40	Calcite	S2	−15.61	14.77	−2.98	4.32
ZK10405-41-1	Calcite	S2	−12.56	17.92	−4.21	7.46
ZK10405-46	Calcite	S2	−16.50	13.85	−1.94	3.40

$1000\ \ln\alpha\ (\text{Calcite-}H_2O) \approx \delta^{18}O_{Calcite} - \delta^{18}O_{H2O} = 2.78 \times 106/(T + 273.15)^2 - 3.39$ (Friedman and O'Neil, 1977).

maximum: 110 °C; Jørgenson et al., 1992), (ii) reducing gases (e.g., CH_4, C_2H_6) were detected in fluid inclusion of sphalerite and calcite, which promote the H_2S produced from SO by reaction of $SO + 2H^+ + CH_4 = CO_2 + H_2S + H_2O$ (Machel et al., 1995) and (iii) the relatively lighter C isotope value (<-4.0‰) measured in this study likely suggested the organic matter is involved in the thermochemical reduction reaction. Therefore, we propose that the near-close system TSR played an important role in the formation of the S^{2-} during the sulfide precipitation in the Zhugongtang deposit. Indeed, evaporitic sulfates extensively occur within carbonate sequences of the western margin of the Yangtze Block (e.g. Liu and Lin, 1999; Ren et al., 2018), which are an important sulfur source of the carbonate-hosted Zn-Pb deposits such as Shaojinwan, Huize, Maoping, Nayongzhi, Maozu and Wusihe in the SYGMP (Fig. 10c; Li et al., 2006; Zhou et al., 2013a,b, 2018; Jin et al., 2016; Xiong et al., 2018; Luo et al., 2020; Wei et al., 2020).

6.2.2. *Evidence from in-situ Pb isotopes*

As shown in Fig. 11a and b, data for in-situ Pb isotope of the analyzed samples plot well above the average upper crustal Pb growth curve of Cumming and Richards (1975) and Stacey and Kramers (1975). Their high $^{207}Pb/^{204}Pb$ and $^{208}Pb/^{204}Pb$ ratios (Fig. 11a and b) suggested the Pb of Zhugongtang was derived from ancient reservoirs and/or possibly lower crustal sources having elevated Th/U ratios (Bouabdellah et al., 2012). The linear trend of Pb isotope data for galena throughout the paragenetic sequence may reflect either a single compositionally homogeneous isotopic reservoir or two well-mixed sources characterized by different Pb isotope ratios (Zartman and Doe, 1981). In view of the measured Pb isotope ratio varying more than twice 2δ analytical uncertainty, the observed linear array displayed by the galena grains supports the mixing of diverse Pb sources rather than the analytical mass fractionation. Therefore, the linear trend of Pb isotopic ratios (Fig. 11a and b) suggests the mixing between two contrasting Pb source endmembers.

Moreover, the distribution of Pb isotope compositions, plot into the overlapping field of the age-corrected (ca. 200 Ma, see Section 6.4) Proterozoic metamorphic basement (Kunyang/Huili Group) and the ore-bearing sedimentary strata (Devonian and Permian), suggesting that the Pb was derived from the mixing of the basement rocks and the country rocks. The two endmembers mixing model is supported by the Pb isotope data from different stages. The early ore-stage galena has relatively lower Pb isotope ratios relative to the late ore-stage (Fig. 11a and b), suggesting the less radiogenic endmembers (the basement rocks) contribute more Pb in the early ore-stage. The higher Pb isotope ratio S2 galena suggests less input from the basement rocks with more contribution from the radiogenic endmembers (such as sedimentary strata). In fact, relatively higher Pb isotope ratios have been reported in ore-bearing sedimentary strata (Devonian and Permian) in the studied region (Fig. 11d). Geological evidence for progressively enhanced water–rock interaction from the early to late ore-stage also favor that country rocks contributed more Pb during the late precipitated sulfides. Given the low abundances of Pb and Zn (average Pb and Zn contents of 10 ppm and 50 ppm, respectively, data from Zhou, 1996), the country rocks are unlikely to contribute enough Pb. Therefore, it is unlikely that large variations of Pb isotope ratios were observed at Zhugongtang.

Based on these relationships and metal contents, we conclude that the Pb, and by inference other metals in the Zhugongtang district, were derived through the mixing of at least two main source-rock reservoirs characterized by distinct Pb isotope compositions with less radiogenic Pb sourced from the basement rocks and radiogenic Pb from host rocks. The mineralizing process involved a hydrothermal fluid that leached metals from the Proterozoic basement metamorphic rocks (including volcanic rocks and siliceous sedimentary rocks) with a quantitatively significant proportion of the metals extracted from the country rocks by fluid-rock interaction.

6.3. *Mechanisms of sulfide precipitation*

Three common metal precipitation mechanisms are proposed for

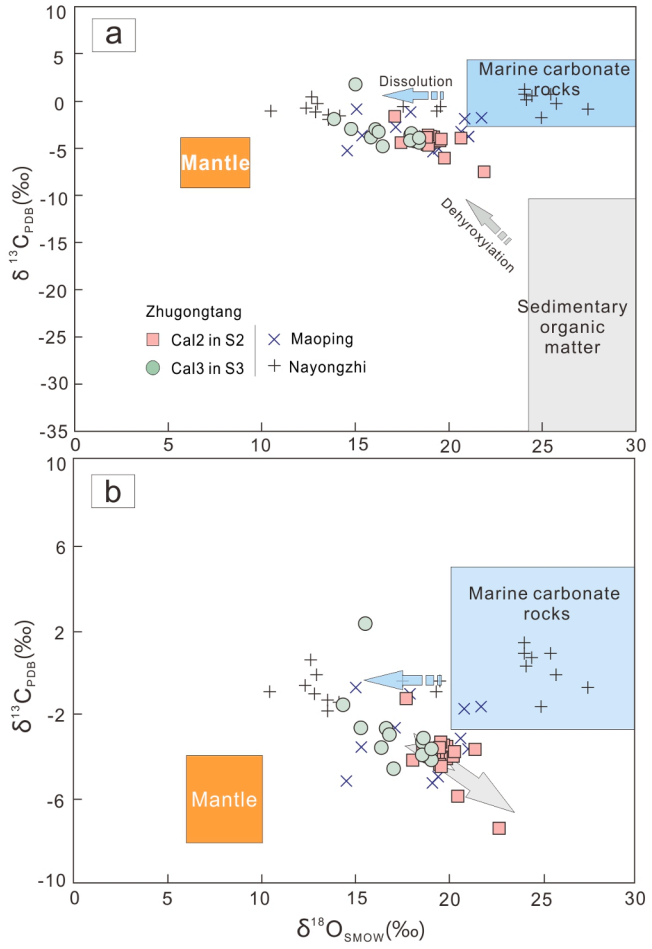

Fig. 9. Binary plot of $\delta^{13}C_{PDB}$ vs. $\delta^{18}O_{SMOW}$ isotopic data for two ore-stages calcite from the Zhugongtang deposit and Nayongzhi and Maoping deposits in the SYGMP (modified from Demény et al., 1998). The C-O isotope data of Nayongzhi and Maoping deposits from Wei (2018) and He et al. (2020).

sulfides in sediment-hosted base metal deposits, such as (i) the reduced sulfur model, (ii) the local sulfate reduction model and (iii) the fluid mixing model (e.g., Sverjensky, 1986; Leach et al., 2005 and references therein). In the reduced sulfur model, reduced sulfur and metals are transported together in an acidic fluid at temperature >200 °C. The deposition of sulfide occurs due to cooling, pH change and/or dilution (Anderson, 1973; Sverjensky, 1986). In the local sulfate reduction model, sulfate and metals are transported in the same fluid. The precipitation of the ore occurs during the sulfate reduction at the deposition site. In the two-fluid mixing model, metal-bearing fluid and reduced sulfur-rich fluid are transported separately via two fluids. Sulfides are precipitated because of two fluids mixing at the site of ore deposition. At Zhugongtang, the reduced sulfur model could be ruled out because of the high pH (>5.5) of the predicted mineralizing solution (as suggested by the presence of K-feldspar) and hence the metals and reduce sulfur could not be delivered from a single fluid (e.g., Sverjensky, 1986). Similarly, the S-Pb isotopic data do not support the local sulfate reduction model. The reduced sulfur was originated from the evaporitic sulfates (in ore-bearing strata) via TSR whilst Pb was mainly derived from basement rocks (see above). This finding is also supported by lighter C isotope (<+4.0‰) of hydrothermal calcite relative to carbonate rocks. Therefore, the two-fluid mixing model is considered as the viable sulfide precipitation mechanism for the Zhugongtang deposit.

Table 4
In-situ S isotope composition of sulfides from the Zhugongtang deposit.

Sample no.	Hosting strata	Analysis spot	Mineral	Stage	$\delta^{32}S$	2δ
ZGT-KB-1	Devonian	spot 1	Sp	S1	22.9	0.2
	Devonian	spot 2	Sp	S1	23.1	0.2
	Devonian	spot 3	Gn	S1	23.3	0.2
	Devonian	spot 4	Py	S1	23.8	0.2
	Devonian	spot 5	Sp	S1	23.4	0.2
	Devonian	spot 6	Sp	S1	22.6	0.2
	Devonian	spot 7	Py	S1	23.3	0.2
	Devonian	spot 8	Gn	S2	18.5	0.2
ZGT-F-1	Devonian	spot 1	Sp	S2	21.4	0.2
	Devonian	spot 2	Gn	S2	19.1	0.2
	Devonian	spot 3	Sp	S2	19.2	0.2
	Devonian	spot 4	Sp	S2	19.1	0.2
ZGT-1	Permian	spot 1	Sp	S2	13.9	0.2
	Permian	spot 2	Sp	S1	14.2	0.2
	Permian	spot 3	Sp	S2	14.0	0.2
	Permian	spot 4	Sp	S1	14.2	0.2
	Permian	spot 5	Sp	S2	14.1	0.2
	Permian	spot 6	Sp	S1	14.1	0.2
	Permian	spot 7	Sp	S1	14.0	0.2
	Permian	spot 8	Sp	S1	14.2	0.2
ZK10405-8	Permian	spot 1	Py	S2	12.9	0.2
	Permian	spot 2	Gn	S2	13.5	0.2
	Permian	spot 3	Py	S2	13.3	0.2
ZK10405-16	Permian	spot 4	Gn	S2	12.2	0.2
	Permian	spot 5	Sp	S1	14.1	0.3
	Permian	spot 6	Sp	S2	13.3	0.1
	Permian	spot 7	Gn	S2	13.3	0.2
	Permian	spot 8	Sp	S2	13.4	0.3
ZK10405-24	Permian	spot 1	Sp	S1	14.4	0.3
	Permian	spot 2	Sp	S1	14.8	0.3
	Permian	spot 3	Py	S1	14.7	0.2
	Permian	spot 4	Sp	S1	14.5	0.1
	Permian	spot 5	Py	S1	15.3	0.2
	Permian	spot 6	Py	S1	15.3	0.2
	Permian	spot 7	Py	S1	15.3	0.2
	Permian	spot 8	Sp	S1	14.0	0.1
ZK10405-30	Permian	spot 1	Gn	S2	12.8	0.2
	Permian	spot 2	Sp	S2	13.9	0.1
	Permian	spot 3	Sp	S1	14.2	0.1
	Permian	spot 4	Py	S1	14.2	0.2
	Permian	spot 5	Py	S1	14.4	0.2
	Permian	spot 6	Sp	S2	13.7	0.2
ZK10405-33	Permian	spot 1	Sp	S1	13.9	0.2
	Permian	spot 2	Sp	S1	14.4	0.1
	Permian	spot 3	Py	S1	14.5	0.2
	Permian	spot 4	Gn	S2	13.2	0.2
	Permian	spot 5	Sp	S2	13.7	0.2
	Permian	spot 6	Sp	S2	13.9	0.2
ZK10405-38	Permian	spot 1	Sp	S1	14.5	0.2
	Permian	spot 2	Gn	S2	13.1	0.2
	Permian	spot 3	Sp	S2	13.8	0.2
	Permian	spot 4	Sp	S2	13.8	0.2
	Permian	spot 5	Sp	S2	13.9	0.2
	Permian	spot 6	Sp	S1	14.2	0.2
	Permian	spot 7	Sp	S1	14.3	0.2
	Permian	spot 8	Sp	S1	14.5	0.2
ZK10405-43	Permian	spot 1	Sp	S2	13.4	0.2
	Permian	spot 2	Sp	S2	13.9	0.2
	Permian	spot 3	Sp	S1	14.5	0.2
	Permian	spot 4	Py	S1	13.9	0.2
ZK10405-58	Permian	spot 1	Py	S1	13.5	0.2
	Permian	spot 2	Py	S2	12.5	0.2
	Permian	spot 3	Gn	S2	12.9	0.2

Note: Py = pyrite; Gn = galena; Sp = sphalerite

6.4. Timing of mineralization

The timing of Zn-Pb mineralization at Zhugongtang has not been well determined due to the lack of reliable geochronological data. Geological and paragenetic relationships suggest that the Zhugongtang deposit is epigenetic and controlled by the NW-trending thrust and fold system, indicating the formation of the thrust faults (e.g., F1, F2) were used to estimate the relative time of mineralization. As shown in Fig. 4a

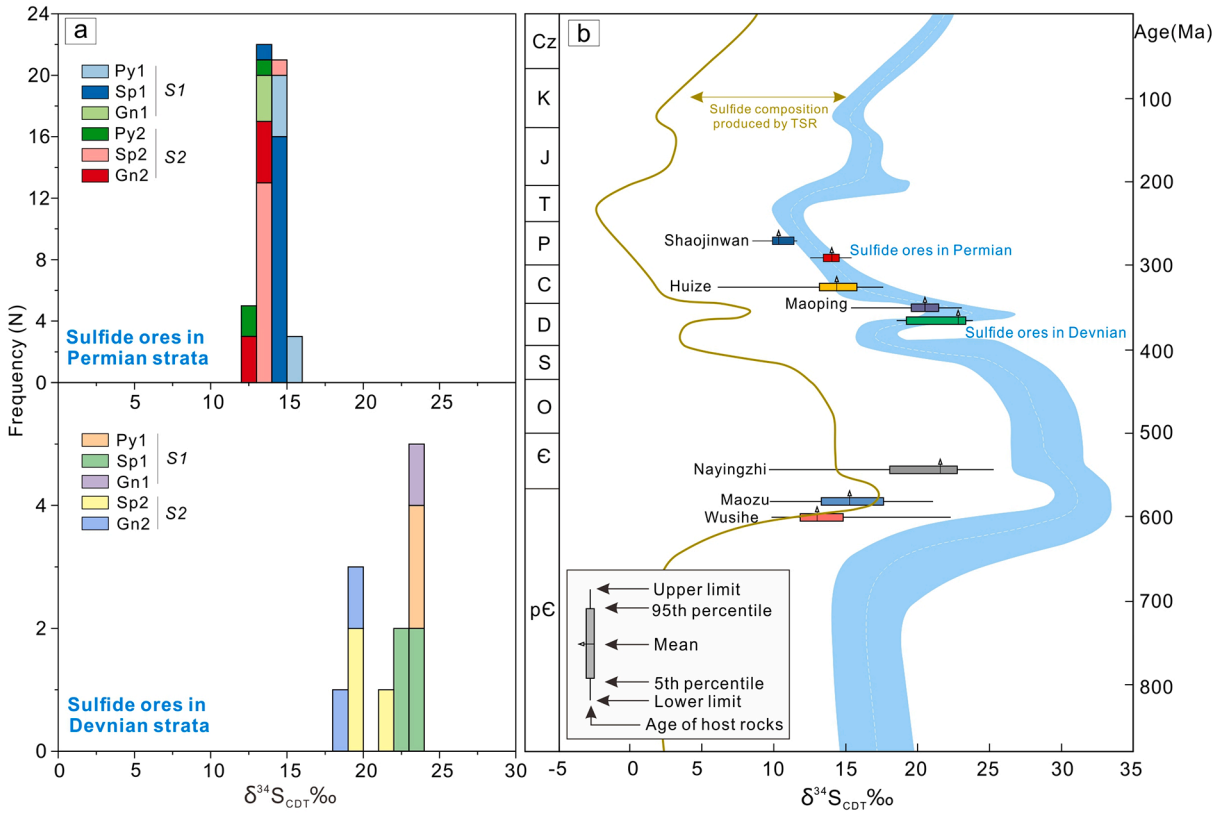

Fig. 10. Sulfur isotopic compositions histogram for sulfides hosted in the strata of Permian (a) and Devonian (b). (c) Diagram illustrating the range and median $\delta^{34}S$ value of sulfides in the typical Zn-Pb deposits in the SYGMP. The marine sulfate composition curve is modified from Farquhar et al. (2010). The pale-brown line indicates the possible range of sulfide composition produced by TSR of seawater-derived sulfate at 150 °C (Kiyosu and Krouse, 1990). The sulfur data of typical Zn-Pb deposit sourced from Li et al. (2006), Zhou et al. (2013a,b), Jin et al. (2016), Zhou et al. (2018), Xiong et al. (2018), and Luo et al. (2020) and Wei et al (2020).

and b, the F1 faults locally cut through the Late Permian Longtan Fm (overlying the ore host), which places a maximum age of ~252 Ma for the mineralization (Shen et al., 2019). Together, the regional NW-trending fold and thrust system is formed by the compression and uplift during the Late Indosinian orogeny (e.g., Ma et al., 2004; Han et al., 2014). Therefore, the maximum age of sulfide deposition at Zhugongtang is the Late Triassic.

Textural relationships constrain the minimum mineralization age. The ore-controlling faults were segmented by post-dates NE- and NS-trending faults that formed during the early Yanshanian (Han et al., 2014). This is supported by the orebodies crosscut by diabase dyke (~165 Ma) in the studies area (Wang et al., 2012). Consequently, a middle Jurassic age (~165 Ma) can be used as a minimum time for mineralization. Moreover, the Tiaoqiao deposit controlled by Ziyun–Yadu fault belt (similar to Zhugongtang) has an Rb-Sr isotopic age of 191.9 ± 6.9 Ma (Zhou et al., 2013a,b), which broadly matches those of the nearby Zn-Pb deposits (225–192 Ma) (e.g., Huang et al., 2004; Li et al., 2007; Zhang et al., 2015 and references therein). Based on this evidence, it is concluded that the Zhugongtang deposit was formed during the Late Triassic to Early Jurassic and related to the Indosinian orogeny in the studies area.

6.5. Implication from ore genesis and the proposed Metallogenic model

The Zhugongtang deposit is hosted in the carbonate rocks of the Late Permian Qixia and Devonian Yaosuo-Wangchengpo Fms and structurally controlled by fold and thrust system formed during Indosinian Orogeny, suggesting an epigenetic origin. In-situ trace elements and oxygen isotope data indicate the hydrothermal fluid in Zhugongtang displays a low-temperature (100–250 °C), low fO_2 and weakly acidic (pH > 5.5) basinal brine character. The ore-forming components in the Zhugongtang deposit involved the country rocks, evaporates in ore-bearing strata, as well as the Proterozoic metamorphic rocks. The main geological and geochemical characteristics can be compared with those of MVT deposits in the orogenic thrust belts worldwide (Table S2). Hence, we propose the Zhugongtang deposit may be an MVT deposit formed in the thrust belts.

The Zhugongtang deposit, one of the typical thrust-controlled Zn-Pb deposits in the SYGMP, has significant implications for the regional Zn-Pb mineralization. Geological and geophysical evidence suggest that the Zhugongtang deposit formed between the Late Triassic and Early Jurassic (similar to the age of nearby Zn-Pb deposits; Huang et al., 2004; Li et al., 2007; Lin et al., 2010; Zhang et al., 2015; Tang et al., 2019), a period which contemporaneous with the Indosinian orogenic event in the study area (Cai and Zhang, 2009; Faure et al., 2014). These ages together with the tectonic evolution of the region can be used to formulate a Metallogenic model for Zhugongtang.

Regionally, the blocks of Indochina and South China collided along the southwestern margin of the Yangtze block during the Late Triassic and Early Jurassic (e.g., Cai and Zhang, 2009). This age is comparable with the Indosinian Orogeny in this area in response to the closure of the Paleo-Tethys (e.g., Faure et al., 2014). The orogenic activity caused the formation of Napanjiang and Youjiang foreland basins (located at the margin of the SYG tringle) and developed a series of NW- and NWW-trending fold and thrust systems (e.g., Cai and Zhang, 2009). As shown in Fig. 13, hot and weak acidic basinal brines driven by the Indosinian Orogeny during the Late Triassic to Early Jurassic extracted metallic elements (e.g., Pb, Zn, Cd, etc.) mainly from the basement rocks as suggested by the Pb isotope (this study), forming metal-bearing chloride complexes in hydrothermal fluids. These fluids migrated

Table 5
In-situ Pb isotopic ratios of galena from the Zhugongtang Pb-Zn deposit.

Sample no.	Hosting strata	Altitude	Stage	$^{206}Pb/^{204}Pb$	2δ	$^{207}Pb/^{204}Pb$	2δ	$^{208}Pb/^{204}Pb$	2δ
ZGT-1-01	Devonian		S2	18.755	0.003	15.766	0.002	39.363	0.019
ZGT-1-02	Devonian		S2	18.754	0.003	15.768	0.002	39.362	0.021
ZGT-1-03	Devonian		S2	18.758	0.002	15.769	0.002	39.366	0.015
ZGT-1-04	Devonian		S1	18.729	0.006	15.761	0.007	39.109	0.013
ZGT-1-05	Devonian		S2	18.738	0.006	15.766	0.004	39.279	0.015
ZGT-KB-1-01	Devonian		S1	18.703	0.004	15.767	0.002	39.319	0.014
ZGT- KB-1-02	Devonian		S1	18.704	0.003	15.768	0.002	39.303	0.016
ZGT- KB-1-03	Devonian		S1	18.703	0.004	15.767	0.002	39.311	0.017
ZGT- KB-1-04	Devonian		S1	18.702	0.004	15.767	0.003	39.308	0.018
ZGT- KB-1-05	Devonian		S1	18.701	0.004	15.764	0.002	39.288	0.015
ZK10405-08-01	Permian	1307.8 m	S2	18.702	0.005	15.762	0.002	39.297	0.016
ZK10405-08-02	Permian	1307.8 m	S1	18.696	0.007	15.764	0.003	39.196	0.009
ZK10405-08-03	Permian	1307.8 m	S2	18.703	0.004	15.764	0.002	39.329	0.007
ZK10405-08-04	Permian	1307.8 m	S1	18.696	0.003	15.761	0.002	39.165	0.016
ZK10405-08-05	Permian	1307.8 m	S2	18.703	0.002	15.764	0.002	39.304	0.017
ZK10405-16-01	Permian	1316.2 m	S1	18.582	0.003	15.757	0.002	39.061	0.005
ZK10405-16-02	Permian	1316.2 m	S1	18.580	0.003	15.758	0.002	39.116	0.017
ZK10405-16-03	Permian	1316.2 m	S1	18.566	0.004	15.759	0.002	39.118	0.006
ZK10405-16-04	Permian	1316.2 m	S1	18.577	0.002	15.759	0.002	39.105	0.015
ZK10405-16-05	Permian	1316.2 m	S1	18.589	0.001	15.759	0.001	39.096	0.020
ZK10405-25-01	Permian	1335.4 m	S2	18.687	0.002	15.764	0.002	39.292	0.008
ZK10405-25-02	Permian	1335.4 m	S1	18.673	0.004	15.758	0.003	39.219	0.013
ZK10405-25-03	Permian	1335.4 m	S2	18.684	0.005	15.766	0.003	39.265	0.014
ZK10405-25-04	Permian	1335.4 m	S2	18.675	0.003	15.763	0.002	39.252	0.016
ZK10405-25-05	Permian	1335.4 m	S2	18.661	0.002	15.764	0.002	39.236	0.018
ZK10405-30-01	Permian	1342.6 m	S1	18.626	0.002	15.761	0.002	39.171	0.017
ZK10405-30-02	Permian	1342.6 m	S1	18.624	0.003	15.757	0.002	39.182	0.008
ZK10405-30-03	Permian	1342.6 m	S1	18.641	0.003	15.762	0.002	39.203	0.012
ZK10405-30-04	Permian	1342.6 m	S1	18.642	0.002	15.762	0.002	39.209	0.010
ZK10405-30-05	Permian	1342.6 m	S1	18.623	0.002	15.760	0.002	39.166	0.017
ZK10405-33-01	Permian	1347.9 m	S2	18.638	0.003	15.762	0.002	39.192	0.019
ZK10405-33-02	Permian	1347.9 m	S2	18.638	0.003	15.762	0.002	39.205	0.013
ZK10405-33-03	Permian	1347.9 m	S1	18.635	0.003	15.763	0.002	39.186	0.022
ZK10405-33-04	Permian	1347.9 m	S2	18.635	0.002	15.760	0.002	39.195	0.019
ZK10405-33-05	Permian	1347.9 m	S2	18.636	0.003	15.758	0.002	39.206	0.007

along the regional deep-seated Ziyun–Yadu fault belt into the pre-karst caves, unconformities and interlayered fault zones of the carbonate rocks sequences at the Zhugongtang district. This is supported by the presence of K-feldspar that needs the flux of external fluid hydrothermal fluid into high porosity carbonate rocks. At the site of deposition, when the fluid encountered the reduced sulfur-rich fluid (trapped from the aquifer of host rock) generated through near-close system TSR, with a drastic change of pH, temperature and other factors resulting in a sharp reduction in the metal solubility by decoupling the Fe and Zn, Pb complexation with Cl. This eventually caused sulfide deposition from ore fluids following the equation (1) $(MeCl(aq) + H_2S(aq) = MeS(s) + H^+ + 4Cl^-$, where Me is Fe, Zn, Pb, etc.). The H^+ generated during reaction (1) would cause carbonate dissolution surrounding wall rock $(4H^+ + CaMg(CO_3)_2(s) \rightarrow 2H_2O(aq) + 2CO_2(aq) + Ca^{2+} + Mg^{2+})$, thereby providing new space for further sulfide precipitation during ore-forming processes. The process gives a rational explanation for the more radiogenic Pb isotopic ratios observed at the later ore-stage galena rather than that of the early ore-stage. In the initial stage of the fluid mixing, abundant pyrite precipitated and elements such as Zn, Pb, Sb and Ag reside in the hydrothermal fluid due to the lack of the optimal physicochemical conditions (e.g., Yardley, 2005; Zhong et al., 2015). When the hydrothermal fluid evolved into the late ore-stage, sphalerite and galena synchronously precipitated with Py2, resulting in a decrease of the Pb and Zn concentrations in Py2 relative to that of Py1 (Fig. 8), supported by the trace elements in pyrite.

7. Conclusions

The Zhugongtang deposit is hosted in the thrust faults and their interlayer fracture zones and the formation of sulfide ore is slightly younger than the thrust faults of the late Indosinian Orogeny.

In-situ trace elements in pyrite and bulk C-O isotopes suggest that the hydrothermal fluid is low-temperature (100–250 °C), low fO_2 and weakly acidic (pH > 5.5) basinal brine and the C was derived from the mixing of the surrounding limestone with a small contribution from organic matter.

In-situ S-Pb isotopic data indicate that the reduced S originated from synchronous seawater sulfates and/or evaporitic sulfates in the ore-bearing strata via thermal-chemical sulfate reduction in the near-close system, whilst the metals were derived from Proterozoic basement metamorphic rocks with a quantitatively significant proportion of the metals extracted from the country rocks by fluid-rock interaction.

The Zhugongtang deposit can be correlated to the MVT deposit formed in the orogenic thrust belts where the mixing between two fluids played a vital role in the formation of the Zn-Pb deposit.

Our results from this newly discovered Zn-Pb deposit in the SYGMP can be extended to understand provide new the ore genesis and ore-forming process of MVT Zn-Pb deposits in the orogenic thrust belt surrounding the Yangtze Block and elsewhere.

CRediT authorship contribution statement

Chen Wei: Conceptualization, Investigation, Methodology, Data Curation, Writing-Original Draft. **Zhilong Huang and Lin Ye:** Funding acquisition, Project administration, Supervision, Validation. **Yusi Hu:** Funding acquisition, Formal Analysis, Data Curation. **M. Santosh:** Writing - Review & Editing. **Lianglun He:** Resources, Investigation. **Jiawei Zhang:** Investigation, Writing - Review & Editing. **Zhiwei He:** Investigation, Resources. **Zhenzhong Xiang:** Methodology. **Da Chen:** Investigation. **Chuanwei Zhu:** Writing - Review & Editing. **Zhongguo Jin:** Investigation.

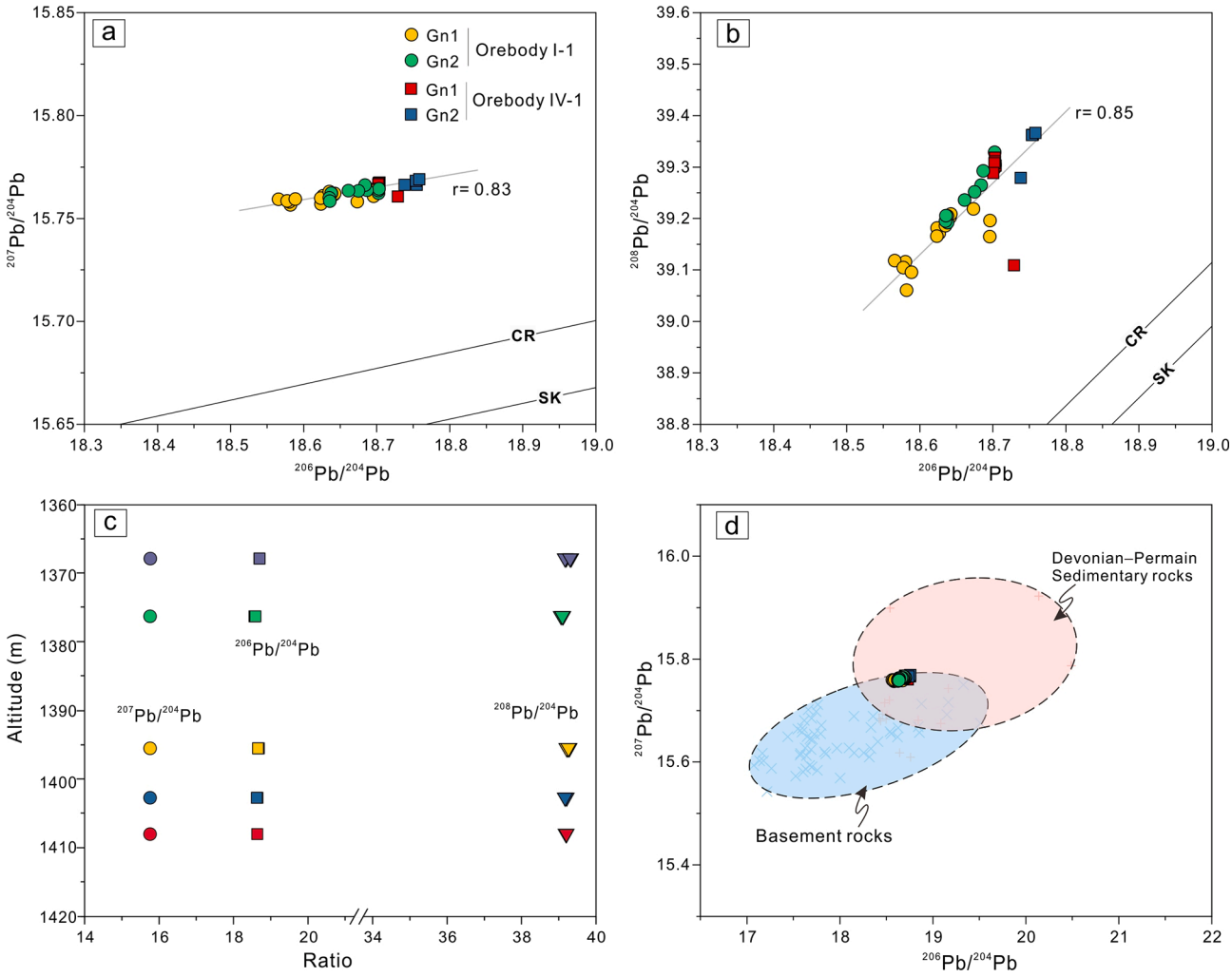

Fig. 11. Pb isotopic ratios of galena from the Zhugongtang deposit. (a) $^{207}Pb/^{204}Pb$ vs. $^{206}Pb/^{204}Pb$ diagram. (b) $^{208}Pb/^{204}Pb$ vs. $^{206}Pb/^{204}Pb$ diagram. (c) The diagram of $^{207}Pb/^{204}Pb$, $^{206}Pb/^{204}Pb$, $^{208}Pb/^{204}Pb$ ratios vs. altitude of selected galena samples. (d) Age-corrected $^{207}Pb/^{204}Pb$ vs. $^{206}Pb/^{204}Pb$ diagram of whole rocks (ca. 200 Ma) associated with the Zhugongtang deposit based on the timing of mineralization in the SYGMP (e.g., Zhang et al., 2015; Zhou et al., 2018). CR and SK: evolution curves for average crustal Pb after Cumming and Richards (1975) and Stacey and Kramers (1975), respectively. The Pb isotope compositions of the metamorphic basement rocks, Devonian to Permian sedimentary rocks are from Chang et al (1997), Liu and Lin (1999), Fu (2004) and Zhou et al. (2013a,b).

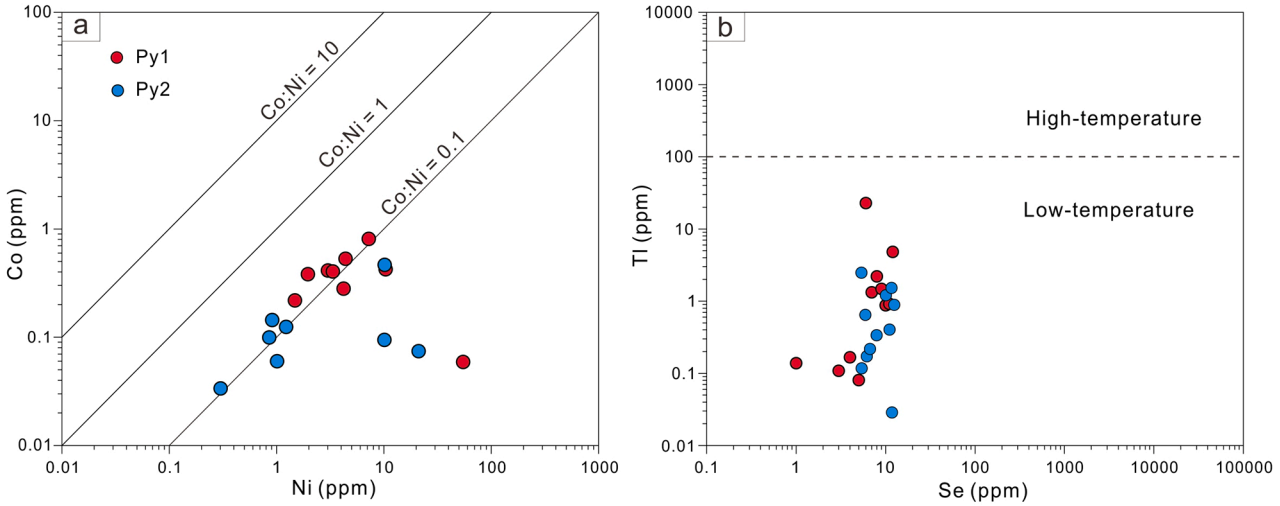

Fig. 12. The diagram of (a) Ni vs. Co and (b) Se vs. Tl for pyrite from Stage 1–2 determined by LA-ICPMS from the Zhugongtang deposit. The high- and low-temperature division is after Maslennikov et al. (2009).

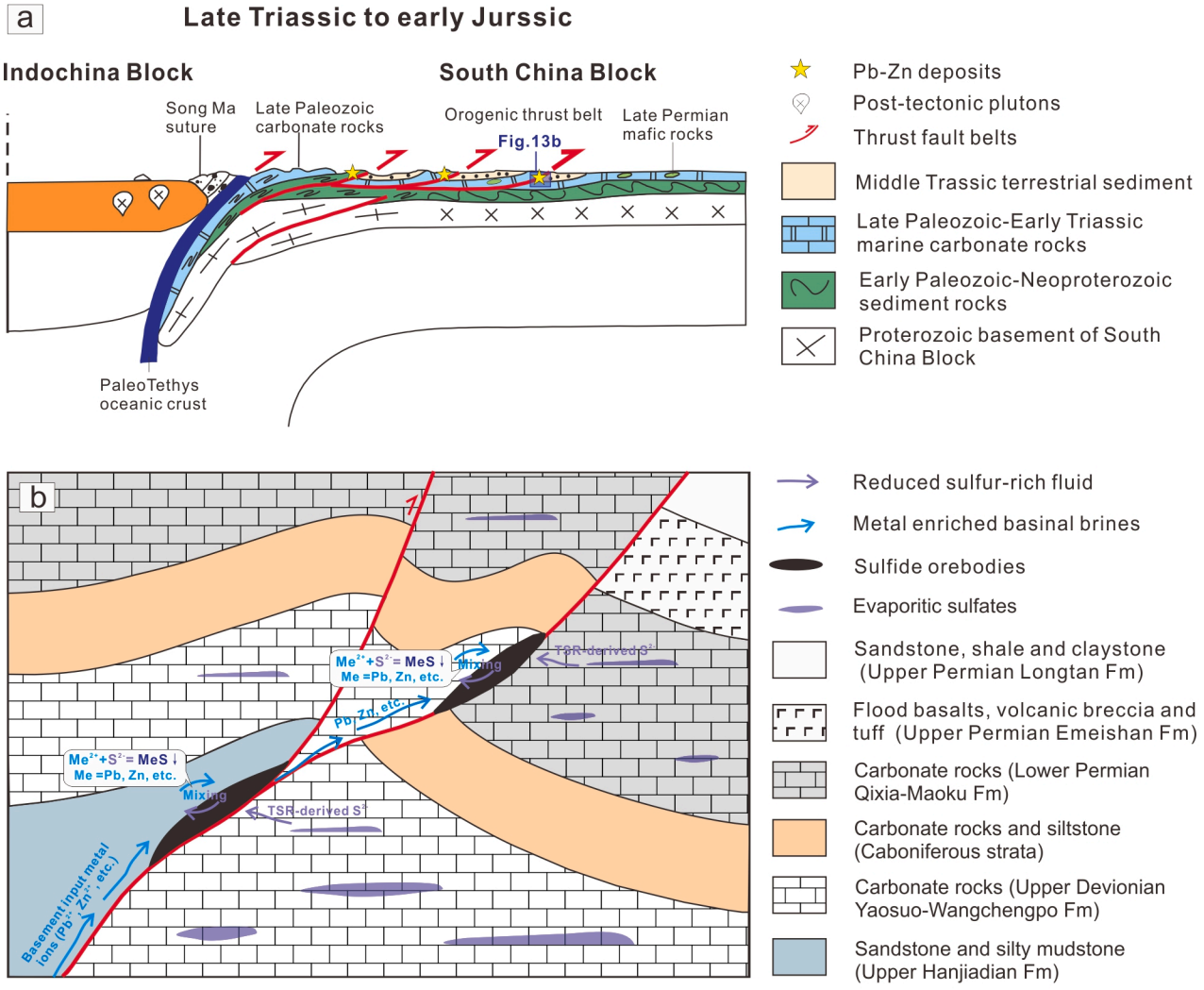

Fig. 13. (a) Geodynamic model of the continental collision between Indochina Block and South China Block (modified after Faure et al., 2014). (b) Schematic model for the genesis of carbonate-hosted Zhugongtang Zn-Pb deposits in the SYGMP, showing the detailed ore deposition process. The basement-derived fluid ascends along the thrust faults and mixes with H_2S-rich fluid (trapped in the sedimentary strata) within the fault-bend folding. A drastic change of pH, temperature and other factors resulted in sulfide deposition from the ore fluid.

Declaration of Competing Interest

The authors declare that they have no known competing financial interests or personal relationships that could have appeared to influence the work reported in this paper.

Acknowledgment

This research project was financially supported by the Natural Science Foundation of Guizhou ([2021]123, [2019]1459), the National Natural Science Foundation of China (U1812402 and 41673056) and the National Key R&D Program of China (2017YFC0602502). The authors are greatly indebted to the Hezhang Bureau of Natural Resources and Guizhou Dingshengxin Mining Development Co., Ltd for their permission to investigate and field sampling the Zhugongtang Zn-Pb deposit. Dr. Jing Gu at IGCAS and Kaiyun Chen at Northwestern University, China are appreciated their assistance in instrumental analysis.

Appendix A. Supplementary material

Supplementary data to this article can be found online at https://doi.org/10.1016/j.jseaes.2021.104914.

References

Anderson, G.M., 1973. The hydrothermal transport and deposition of galena and sphalerite near 100°C. Econ. Geol. 68, 480–492.
Anderson, G.M., Macqueen, R.W., 1982. Ore deposit models 6 Mississippi Valley-type lead-zinc deposits. Geosci. Can. 9, 108–117.
Appold, M.S., Garven, G., 1999. The hydrology of ore formation in the southeast Missouri district: Numerical models of topography-driven fluid flow during the Ouachita orogeny. Econ. Geol. 94, 913–936.
Bau, M., Romer, R.L., Lüders, V., Dulski, P., 2003. Tracing element sources of hydrothermal mineral deposits: REE and Y distribution and Sr-Nd-Pb isotopes in fluorite from MVT deposits in the Pennine orefield, England. Miner. Deposita 38 (8), 992–1008.
Bouabdellah, M., Sangster, D.F., Leach, D.L., Brown, A.C., 2012. Genesis of the Touissit-Bou Beker Mississippi Valley-type district Morocco-Algeria, and its relationship to the Africa-Europe collision. Econ. Geol. 107, 117–146.
Bradley, D.C., Leach, D.L., 2003. Tectonic controls of Mississippi Valley-type lead-zinc mineralization in orogenic forelands. Miner. Deposita 38 (6), 652–667.
Bralia, A., Sabatini, G., Troja, F., 1979. A revaluation of the Co/Ni ratio in pyrite as geochemical tool in ore genesis problems. Miner. Deposita 14, 353–374.
Cai, J.-X., Zhang, K.-J., 2009. A new model for the Indochina and South China collision during the Late Permian to the Middle Triassic. Tectonophysics 467 (1-4), 35–43.
Cawood, P.A., 2005. Terra Australis Orogen: Rodinia breakup and development of the Pacific and Iapetus margins of Gondwana during the Neoproterozoic and Paleozoic. Earth-Science. Rev. 69 (3-4), 249–279.
Chang, X.Y., Zhu, B.Q., Sun, D.H., Qiu, H.N., Zou, R., 1997. Isotope geochemistry study of Dongchuan copper deposits in middle Yunnan province, SW China, 1.

Stratigraphic chronology and application of geochemical exploration by lead isotopes. Geochimica 26, 32–38 (in Chinese with English abstract).
Chen, L.u., Chen, K., Bao, Z., Liang, P., Sun, T., Yuan, H., 2017. Preparation of standards for in situ sulfur isotope measurement in sulfides using femtosecond laser ablation MC-ICP-MS. J. Anal. Atom. Spectrom. 32 (1), 107–116.
Claypool, G.E., Holser, W.T., Kaplan, I.R., Sakai, H., Zak, I., 1980. The age curves of sulfur and oxygen isotopes in marine sulfate and their mutual interpretation. Chem. Geol. 28, 199–260.
Cumming, G.L., Richards, J.R., 1975. Ore lead isotope ratios in a continuously changing earth. Earth Planet. Sci. Lett. 28 (2), 155–171.
Danyushevsky, L., Robinson, P., Gilbert, S., Norman, M., Large, R., McGoldrick, P., Shelley, M., 2011. Routine quantitative multi-element analysis of sulphide minerals by laser ablation ICP-MS: standard development and consideration of matrix effects. Geochem. Explor. Environ. Anal. 11 (1), 51–60.
Dong, Y., Liu, X., Santosh, M., Chen, Q., Zhang, X., Li, W., He, D., Zhang, G., 2012. Neoproterozoic accretionary tectonics along the northwestern margin of the Yangtze Block, China: constraints from zircon U-Pb geochronology and geochemistry. Precambrian Res. 196-197, 247–274.
Farquhar, J., Wu, N.P., Canfield, D.E., Oduro, H., 2010. Connections between sulfur cycle evolution, sulfur isotopes, sediments, and base metal VMS, SEDEX, and MVT deposits. Econ. Geol. 105, 509–533.
Faure, M., Lepvrier, C., Nguyen, V.V., Vu, T.V., Lin, W., Chen, Z., 2014. The South China block-Indochina collision: where, when, and how? J. Asian Earth Sci. 79, 260–274.
Zhou, J.-X., Xiang, Z.-Z., Zhou, M.-F., Feng, Y.-X., Luo, K., Huang, Z.-L., Wu, T., 2018. The giant Upper Yangtze Pb-Zn province in SW China: reviews, new advances and a new genetic model. J. Asian Earth Sci. 154, 280–315.
Friedman, I., O'Neil, J.R., 1977. Compilation of stable isotope fractionation factors of geochemical interest. Data of Geochemistry. U.S. Geological Survey Professional Paper, 440, 1–12.
Fu, S.H., 2004. Metallogenesis of Pb–Zn deposits and enrichment regularity of dispersed elements Cd, Ga, and Ge in SW Yangtze Block. A Dissertation submitted to Chengdu University of Technology Ph.D. Degree, Chengdu University of Technology, Chengdu, pp. 1–83 (in Chinese with English abstract).
Han, R.S., Hu, Y.Z., Wang, X.K., Hou, B.H., Huang, Z.L., Chen, J., Wang, F., Wu, P., Li, B., Wang, H.J., Dong, Y., Lei, L., 2012. Mineralization model of rich Ge–Ag-bearing Zn–Pb polymetallic deposit concentrated district in northeastern Yunnan, China. Acta. Geol. Sin-Engl. 86, 280–294 (in Chinese with English abstract).
Han, R.S., Wang, F., Hu, Y.Z., Wang, X.K., Ren, T., Qiu, W.L., Zhong, K.H., 2014. Metallogenic tectonic fynamics and chronology constrains on the Huize-type HZT, Germanium-rich silver-zinc-lead deposits. Geotect. et. Metall. 38, 758–771.
Hannington, M.D., Jonasson, I.R., Herzig, P.M., Petersen, S., 1995. Physical, chemical processes of seafloor mineralization at mid-ocean ridges. Geophy. Monog. 91, 115–157.
He, B., Xu, Y.-G., Huang, X.-L., Luo, Z.-Y., Shi, Y.-R., Yang, Q.-J., Yu, S.-Y., 2007. Age and duration of the Emeishan flood volcanism, SW China: geochemistry and SHRIMP zircon U-Pb dating of silicic ignimbrites, post-volcanic Xuanwei Formation and clay tuff at the Chaotian section. Earth Planet. Sc. Lett. 255 (3-4), 306–323.
He, Y., Wu, T., Huang, Z., Ye, L., Deng, P., Xiang, Z., 2020. Genesis of the Maoping carbonate-hosted Pb–Zn deposit, northeastern Yunnan Province, China: evidences from geology and C-O–S–Pb isotopes. Acta Geochim 39 (5), 782–796.
He, L.L., Wu, D.W., Zhao, F., Jin, X.L., Bai, G.H., Chen, Z.X., Wang, J., Huang, Q., Cai, J. C., 2019. Geological characteristics, exploration model and prospecting direction of the Zhugongtang Ultra-large Pb-Zn deposit in Guizhou Province. Guizhou Geol. 26, 101–109 (in Chinese with English abstract).
Heijlen, W., Muchez, P., Banks, D.A., Schneider, J., Kucha, H., Keppens, E., 2003. Carbonate-hosted Zn-Pb deposits in Upper Silesia, Poland: Origin and evolution of mineralizing fluids and constraints on genetic models. Econ. Geol. 98 (5), 911–932.
Hoefs, J., 2009. Stable Isotope Geochemistry, sixth ed., Springer-Verlag, doi: 10.1007/978-3-540-70708-0.
Huang, Z.L., Chen, J., Han, R.S., Li, W.B., Liu, C.Q., Zhang, Z.L., Ma, D.Y., Gao, D.R., Yang, H.L., 2004. Geochemistry and ore-formation of the Huize giant lead-zinc deposit, Yunnan Province, China: Discussion on the relationship between Emeishan flood basalts and lead-zinc mineralization. Geol. Pub. House, Beijing, 1–154 (in Chinese).
Jin, Z.G., Zhou, J.X., Huang, Z.L., Luo, K., Gao, J.G., Peng, S., Wang, B., Chen, X.L., 2016. Ore genesis of the Nayongzhi deposit, Puding City, Guizhou Province, China: evidence from S and in situ Pb isotopes. Acta. Petrol. Sin. 32, 3441–3455 (in Chinese with English abstract).
Jørgenson, B.B., Isaksen, M.F., Jannasch, H.W., 1992. Bacterial sulfate reduction above 100°C in deep sea hydrothermal vent sediments. Science 258, 1756–1757.
Kiyosu, Y., Krouse, H.R., 1990. The role of organic acid in the abiogenic reduction of sulfate and the sulfur isotope effect. Geochem. J. 24 (1), 21–27.
Leach, D.L., Bradley, D., Lewchuk, M.T., Symons, D.T., de Marsily, G., Brannon, J., 2001. Mississippi Valley-type lead-zinc deposits through geological time: implications from recent age-dating research. Miner. Deposita 36 (8), 711–740.
Leach, D.L., Sangster, D.F., Kelley, K.D., Large, R.R., Garven, G., Allen, C.R., Gutzmer, J., Walters, S., 2005. Sediment-hosted lead-zinc deposits: a global perspective. Econ. Geol. Vol, 561–607.
Li, W.B., Huang, Z.L., Zhang, G., 2006. Sources of the ore metals of the Huize ore field in Yunnan province: constraints from Pb, S, C, H, O and Sr isotope geochemistry. Acta Petrol. Sin. 22, 2567–2580 (in Chinese with English abstract).
Li, W., Huang, Z., Yin, M., 2007. Dating of the giant Huize Zn-Pb ore field of Yunnan province, southwest China: constraints from the Sm-Nd system in hydrothermal calcite. Resour. Geol. 57 (1), 90–97.
Li, X.J., Wu, M.D., Duan, J.S., 1984. The stratigraphic sequence of the Kunyang Group and its top and bottom boundaries. Geol. Rev. 30, 399–408 (in Chinese with English abstract).
Li, Z.L., Ye, L., Hu, Y.S., Wei, C., Huang, Z.L., Yang, Y.L., Danyushevsky, L., 2020. Trace elements in sulfides from the Maozu Pb-Zn deposit, Yunnan Province, China: implications for trace-element incorporation mechanisms and ore genesis. Am. Mineral. 1051, 1734–1751.
Li, Z.X., Li, X.H., Wartho, J.A., Clark, C., Li, W.X., Zhang, C.L., Bao, C.M., 2010. Magmatic and metamorphic events during the Early Paleozoic Wuyi-Yunkai Orogeny, southeastern South China: new age constraints and P-T conditions. GSA. Bulletin 1225, 772–793.
Lin, Z.Y., Wang, D.H., Zhang, C.Q., 2010. Rb-Sr isotopic age of sphalerite from the Paoma lead-zinc deposit in Sichuan Province and its implications. Geol. China 37, 488–1196 (in Chinese with English abstract).
Liu, H.C., Lin, W.D., 1999. Regularity research of Ag. Zn. Pb ore deposits northeast Yunnan Province. Yunnan University Press, Kunming, 1–468 (in Chinese).
Liu, Y.-C., Kendrick, M.A., Hou, Z.-Q., Yang, Z.-S., Tian, S.-H., Song, Y.-C., Honda, M., 2017. Hydrothermal fluid origins of carbonate-hosted Pb-Zn deposits of the Sanjiang thrust belt, Tibet: indications from noble gases and halogens. Econ. Geol. 112 (5), 1247–1268.
Luo, K., Zhou, J.X., Huang, Z.L., Caulfield, J., Zhao, J.X., Feng, Y.X., Ouyang, H.G., 2020. New insights into the evolution of Mississippi Valley-Type hydrothermal system: a case study of the Wusihe Pb-Zn deposit, South China, using quartz in-situ trace elements and sulfides in situ S-Pb isotopes. Am. Mineral. 105, 35–51.
Ma, L., Chen, H.J., Gan, K.W., Xu, K.D., Xu, X.S., Wu, G.Y., Ye, Z., Liang, X., Wu, S.H., Qiu, Y.Y., Zhang, P.L., Ge, F.F. 2004. Geotectonic and marine petroleum geology in southern China. Beijing, China. Geol. Pub. House, Beijing, 1–113 (in Chinese).
Machel, H.G., Krouse, H.R., Sassen, R., 1995. Products and distinguishing criteria of bacterial and thermochemical sulfate reduction. Appl. Geochem. 10 (4), 373–389.
Maghfouri, S., Rastad, E., Lentz, D.R., Mousivand, F., Choulet, F., 2018. Mineralogy, microchemistry and fluid inclusion studies of the Besshi-type Nudeh Cu-Zn VMS deposit, Iran. Geochemistry 78 (1), 40–57.
Maslennikov, V.V., Maslennikova, S.P., Large, R.R., Danyushevsky, L.V., 2009. Study of trace element zonation in Vent Chimneys from the Silurian Yaman-Kasy volcanic-hosted massive sulfide deposit Southern Urals, Russia, using laser ablation inductively coupled plasma mass spectrometry LA-ICPMS. Econ. Geol. 104 (8), 1111–1141.
Matcalfe, I., 2002. Permian tectonic framework and palaeogeography of SE Asia. J. Asian Earth Sci. 20 (6), 551–556.
McLimans, R.K., 1977. Geologic, fluid inclusion, and stable isotope studies of the Upper Mississippi zinc-lead district, southwest Wisconsin. Unpub. Ph.D. Thesis. Pennsylvania State University.
Metcalfe, I., 2006. Paleozoic and Mesozoic tectonic evolution and paleogeography of East Asian crustal fragments: The Korean Peninsula in context. Gondwana Res. 9, 24–46.
Muchez, P., Heijlen, W., Banks, D., Blundell, D., Boni, M., Grandia, F., 2005. Extensional tectonics and the timing and formation of basin-hosted deposits in Europe. Ore Geol. Rev. 27, 241–267.
Ohmoto, H., Rye, R.O., 1979. Isotopes of sulfur and carbon. In: Barnes, H.L. (Ed.), Geochemistry of hydrothermal ore deposits, 2nd ed. John Wiley and Sons, New York, pp. 509–567.
Ohmoto, H., 1986. Stable isotope geochemistry of ore deposits. Rev. Mineral. 16, 491–560.
Oyebamiji, A., Hu, R., Zhao, C., Zafar, T., 2020. Origin of the Triassic Qilinchang Pb-Zn deposit in the western Yangtze block, SW China: insights from in-situ trace elemental compositions of base metal sulphides. J. Asian Earth Sci. 192, 104292. https://doi.org/10.1016/j.jseaes.2020.104292.
Partey, F., Lev, S., Casey, R., Widom, E., Lueth, V.W., Rakovan, J., 2009. Source of fluorine and petrogenesis of the Rio Grande rift-type barite-fluorite-galena deposits. Econ. Geol. 104 (4), 505–520.
Ren, S.L., Li, Y.H., Zeng, P.H., Qiu, W.L., Fan, C.F., Hu, G.Y., 2018. Effect of sulfate evaporate salt layer in mineralization of Huize and Maoping lead-zinc deposits in Yunnan: Evidence from sulfur isotope. Acta Geol. Sin. 92, 1041–1055 (in Chinese with English abstract).
Rusk, B.G., Lowers, H.A., Reed, M.H., 2008. Trace elements in hydrothermal quartz: relationships to cathodoluminescent textures and insights into vein formation. Geology 36 (7), 547. https://doi.org/10.1130/G24580A.110.1130/2008132.
Shen, S., Zhang, H., Zhang, Y., Yuan, D., Chen, B.o., He, W., Mu, L., Lin, W., Wang, W., Chen, J., Wu, Q., Cao, C., Wang, Y., Wang, X., 2019. Permian integrative stratigraphy and timescale of China. Sci. China Earth Sci. 62 (1), 154–188.
Singer, D.A., 1995. World class base and precious metal deposits: a quantitative analysis. Econ. Geol. 90, 88–104.
Smethurst, M., Sangster, D., Symons, D., Lewchuk, M., 1999. Paleomagnetic age for Zn-Pb mineralization at Robb Lake, northeastern British Columbia. Bull Can. Petr. Geol. 47, 548–555.
Song, Y.C., Yang, T.N., Zhang, H.R., Liu, Y.C., Hao, H.D., Li, Z., 2015. The Chaqupacha Mississippi Valley-type Pb-Zn deposit, central Tibet: Ore formation in a fold and thrust belt of the India-Asia continental collision zone. Ore Geol. Rev. 70, 533–545.
Stacey, J.S., Kramers, J.D., 1975. Approximation of terrestrial lead isotope evolution by a two-stage model. Earth Planet. Sc. Lett. 26 (2), 207–221.
Sverjensky, D.A., 1986. Genesis of Mississippi Valley-type lead-zinc deposits. Annu. Rev. Planet. Earth Sci. 14, 177–199.
Taylor, H.P., Frechen, J., Degens, E.T., 1967. Oxygen and carbon isotope studies of carbonatites from the Laacher See District, West Germany and the AlnöDistrict, Sweden. Geochim. Cosmochim. Acta 31 (3), 407–430.

Tang, Y.Y., Bi, X.W., Zhou, J.X., Liang, F., Qi, Y.Q., Leng, C.B., Zhang, H., 2019. Rb-Sr isotopic age, S-Pb-Sr isotopic compositions and genesis of the ca. 200Ma Yunluheba Pb-Zn deposit in NW Guizhou Province, SW China. J. Asian Earth Sci. 185, 104054.
Veizer, J., Hoefs, J., 1976. The nature of O^{18}/O^{16} and C^{13}/C^{12} secular trends in sedimentary carbonate rocks. Geochim. Cosmochim. Acta 40 (11), 1387–1395.
Wang, R., Zhang, C.Q., Wu, Y., Wei, C., 2012. The age of diabase in Tianbaoshan Pb–Zn deposit and the genetic relationship between lead-zinc mineralization and the diabase dyke. Miner. Depos. 31, 449–450 (in Chinese).
Wang, Y., Fan, W., Zhang, G., Zhang, Y., 2013. Phanerozoic tectonics of the South China Block: Key observations and controversies. Gondwana Res. 23 (4), 1273–1305.
Wei, C., 2018. Ore-forming fluid and ore genesis of the Nayongzhi deposit in northwestern Guizhou, China. Unpub. M. Sci. thesis, Guiyang, Institute of Geochemistry, Chinese Academy of Sciences (in Chinese with English abstract).
Wei, C., Ye, L., Li, Z.L., Hu, Y.S., Huang, Z.L., Liu, Y.P., Wang, H.Y., 2020. Metal sources and ore genesis of the Wusihe Pb-Zn deposit in Sichuan, China: New evidence from in-situ S and Pb isotopes. Acta Petrol. Sin. 261, 3783–3796 (in Chinese with English abstract).
Wei, C., Ye, L., Hu, Y., Huang, Z., Danyushevsky, L., Wang, H., 2021. LA-ICP-MS analyses of trace elements in base metal sulfides from carbonate-hosted Zn-Pb deposits, South China: a case study of the Maoping deposit. Ore Geol. Rev. 130, 103945.
Wilkinson, J.J., 2010. A review of fluid inclusion constraints on mineralization in the Irish ore field and implications for the genesis of sediment-hosted Zn-Pb deposits. Econ. Geol. 105 (2), 417–442.
Wu, Y., Zhang, C., Mao, J., Ouyang, H., Sun, J., 2013. The genetic relationship between hydrocarbon systems and Mississippi Valley-type Zn–Pb deposits along the SW margin of Sichuan Basin, China. Int. Geol. Rev. 55 (8), 941–957.
Xiong, S.F., Gong, Y.J., Jiang, S.Y., Zhao, X.J., Li, Q., Zeng, G.P., 2018. Ore genesis of the Wusihe carbonate-hosted Zn-Pb deposit in the Dadu River Valley district, Yangtze Block, SW China: evidence from ore geology, S-Pb isotopes, and sphalerite Rb-Sr dating. Miner. Deposita 53, 967–979.
Yan, D.-P., Zhou, M.-F., Song, H., Fu, Z., 2003. Structural style and tectonic significance of the Jianglang dome in the eastern margin of the Tibetan Plateau, China. J. Struct. Geol. 25 (5), 765–779.
Yao, J., Shu, L., Santosh, M., Zhao, G., 2014. Neoproterozoic arc-related mafic-ultramafic rocks and syn-collision granite from the western segment of the Jiangnan Orogen, South China: constraints on the Neoproterozoic assembly of the Yangtze and Cathaysia Blocks. Precambrian Res. 243, 39–62.
Yao, W.-H., Li, Z.-X., 2016. Tectonostratigraphic history of the Ediacaran-Silurian Nanhua foreland basin in South China. Tectonophysics 674, 31–51.
Yardley, B.W., 2005. Metal concentrations in crustal fluids and their relationship to ore formation. Econ. Geol. 100th Anniv, 613–632.
Zartman, R.E., Doe, B.R., 1981. Plumbotectonics—the model. Tectonophysics 75 (1-2), 135–162.
Zhang, C., Wu, Y., Hou, L., Mao, J., 2015. Geodynamic setting of mineralization of Mississippi Valley-type deposits in world-class Sichuan-Yunnan-Guizhou Zn-Pb triangle, southwest China: Implications from age-dating studies in the past decade and the Sm-Nd age of Jinshachang deposit. J. Asian Earth Sci. 103, 103–114.
Zhang, W., Hu, Z., Günther, D., Liu, Y., Ling, W., Zong, K., Chen, H., Gao, S., 2016. Direct lead isotope analysis in Hg-rich sulfides by LA-MC-ICP-MS with a gas exchange device and matrix-matched calibration. Anal. Chim. Acta 948, 9–18.
Zhang, Y.X., Wu, Y., Tian, G., Shen, L., Zhou, Y.M., Dong, W.W., Zeng, R., Yang, X.C., Zhang, C.Q., 2014. Mineralization age and the source of ore-forming material at Lehong Pb-Zn deposit, Yunnan Province: constraints from Rb-Sr and S isotopes system. Acta Mineral Sin. 34, 305–311 (in Chinese with English abstract).
Zheng, Y.F., Chen, J.F., 2000. Stable Isotope Geochemistry. Sci. Press, Beijing, 1–316 (in Chinese).
Zhong, R., Brugger, J., Chen, Y., Li, W., 2015. Contrasting regimes of Cu, Zn and Pb transport in ore-forming hydrothermal fluids. Chem. Geol. 395, 154–164.
Zhou, C.X., 1996, The origin of the mineralizing metals, the geochemical characteristics of ore-forming fluid, and the genesis of Qilinchang Zn-Pb deposit, northeast Yunnan Province, China: Unpublished M. Sci. thesis, Guiyang, Institute of Geochemistry, Chinese Academy of Sciences, pp. 1–112 (in Chinese with English abstract).
Zhou, J., Huang, Z., Zhou, M., Li, X., Jin, Z., 2013a. Constraints of C-O–S–Pb isotope compositions and Rb–Sr isotopic age on the origin of the Tianqiao carbonate-hosted Pb–Zn deposit, SW China. Ore Geol. Rev. 53, 77–92.
Zhou, J., Huang, Z., Bao, G., 2013b. Geological and sulfur–lead–strontium isotopic studies of the Shaojiwan Pb–Zn deposit, southwest China: implications for the origin of hydrothermal fluids. J. Geochem. Explor. 128, 51–61.